CrossMark

Dust-buried Compact Sources in the Dwarf Galaxy NGC 4449

Daniela Calzetti[1] , Sean T. Linden[1] , Timothy McQuaid[1], Matteo Messa[2,3] , Zhiyuan Ji[4] , Mark R. Krumholz[5] ,
Angela Adamo[3] , Bruce Elmegreen[6] , Kathryn Grasha[5] , Kelsey E. Johnson[7] , Elena Sabbi[8] , Linda J. Smith[8] , and
Varun Bajaj[8]

[1] Department of Astronomy, University of Massachusetts Amherst, 710 North Pleasant Street, Amherst, MA 01003, USA; calzetti@astro.umass.edu
[2] Department of Astronomy, Université de Genève, 24 rue du Général-Dufour, 1211 Genève 4, Switzerland
[3] Department of Astronomy, Stockholm University, Stockholm, Sweden
[4] Department of Astronomy, University of Arizona, Tucson, AZ, USA
[5] Research School of Astronomy and Astrophysics, Australian National University, Camberra, Australia
[6] IBM Research Division, T.J. Watson Research Center, Yorktown Heights, NY, USA
[7] Department of Astronomy, University of Virginia, Charlottesville, VA, USA
[8] Space Telescope Science Institute, 3700 San Martin Drive, Baltimore, MD 21218, USA

Abstract

Multiwavelength images from the Hubble Space Telescope covering the wavelength range 0.27–1.6 μm show that the central area of the nearby dwarf galaxy NGC 4449 contains several tens of compact sources that are emitting in the hydrogen recombination line Paβ (1.2818 μm) but are only marginally detected in Hα (0.6563 μm) and undetected at wavelengths $\lambda \lesssim 0.55$ μm. An analysis of the spectral energy distributions (SEDs) of these sources indicates that they are likely relatively young stellar clusters heavily attenuated by dust. The selection function used to identify the sources prevents meaningful statistical analyses of their age, mass, and dust extinction distributions. However, these cluster candidates have ages ~5–6 Myr and $A_V > 6$ mag, according to their SED fits, and are extremely compact, with typical deconvolved radii of 1 pc. The dusty clusters are located at the periphery of the dark clouds within the galaxy and appear to be partially embedded. Density and pressure considerations indicate that the H II regions surrounding these clusters may be stalled, and that pre-supernova (pre-SN) feedback has not been able to clear the clusters of their natal cocoons. These findings are in potential tension with existing models that regulate star formation with pre-SN feedback, since pre-SN feedback acts on short timescales, $\lesssim 4$ Myr, for a standard stellar initial mass function. The existence of a population of dusty stellar clusters with ages >4 Myr, if confirmed by future observations, paints a more complex picture for the role of stellar feedback in controlling star formation.

Unified Astronomy Thesaurus concepts: Young star clusters (1833); Star clusters (1567)

Supporting material: machine-readable tables

1. Introduction

Star formation is the result of contrasting mechanisms acting on the gas in galaxies. Gravity and cooling collapses the gas producing high-density cores, where stars form; feedback from these stars disperses the natal cores, and injects energy and matter into the interstellar medium (ISM) and circumgalactic medium, driving turbulence and maintaining a multiphase ISM (Hennebelle & Chabrier 2011; Hopkins et al. 2012; Dobbs 2015; Goldbaum et al. 2016). The feedback from stars—outflows, radiation, winds, and supernovae (SNe)—regulates star formation either at the local level, by acting directly on the clouds to stop star formation (e.g., Krumholz & McKee 2005; Dobbs et al. 2011; Hopkins et al. 2014; Federrath 2015; Grisdale et al. 2017; Grudić et al. 2018; Krumholz et al. 2019), or at the global level, by maintaining galaxies in a "pseudo-equilibrium" state, thus setting the collapse rate on kiloparsec scales (e.g., Ostriker et al. 2010; Ostriker & Kim 2022). Once the fragmentation of a gas cloud begins, star formation is expected to be a fast process, taking less than a few megayears from the appearance of the first protostars to the disruption of the molecular cloud (e.g., Grudić et al. 2022). The

low efficiency of star formation, at the level of a few percent when integrated over large regions (giant molecular clouds, galaxies, etc.), is a direct consequence of stellar feedback from young, massive stellar populations (Ostriker et al. 2010; Hopkins et al. 2014; Peters et al. 2017; Orr et al. 2018; Ostriker & Kim 2022).

Photoionization, direct and indirect radiation pressure, and stellar winds are all part of massive star feedback and are often bundled under the terminology "pre-supernova (pre-SN) feedback," since they have timescales of a few megayears (Pellegrini et al. 2011; Dale et al. 2012; Krause et al. 2013; Krumholz et al. 2019). Pre-SN feedback helps clear the medium surrounding massive stars before the first SN explosion occurs at around ~4 Myr (Leitherer et al. 2014), and the effect of SN explosions is to mainly inject energy into the ISM outside of the natal cloud, rather than affecting the star formation within the natal cloud itself (Lucas et al. 2020; Grudić et al. 2022). According to models, radiative feedback may be key for regulating star formation within galaxies (Hopkins et al. 2020; Bending et al. 2022) and processes that act over timescales shorter than SN explosions may be required to clear channels in the ISM for the escape of ionizing photons from galaxies, as half of the ionizing photons are supplied within the first 3 Myr (Ma et al. 2020).

Several observational studies support the short timescales of pre-SN feedback as the main mode to regulate star formation.

These studies mainly concentrate on young stellar clusters, as these contain the majority, $\gtrsim 70\%$, of massive stars (Oey et al. 2004) and are therefore primary sites for studying stellar feedback. Combining UV/optical photometry of stellar clusters with Hα morphology of H II regions from the Hubble Space Telescope (HST), several authors have derived clearing timescales <4–5 Myr, and as short as 2 Myr, in nearby galaxies (Whitmore et al. 2011; Hollyhead et al. 2015; Hannon et al. 2019, 2022). However, these studies use UV and optical data, and are thus limited to the relatively dust-free components of star formation. The addition of CO data to trace molecular clouds and, in some cases, 24 μm imaging from the Spitzer Space Telescope to trace the dust-enshrouded star formation has enabled the use of both frequency and positional analysis to derive timescales. Matthews et al. (2018), Grasha et al. (2018, 2019), Kruijssen et al. (2019), Kim et al. (2021), and Chevance et al. (2022) used different techniques to conclude that timescales are short, only 3–5 Myr, and likely shorter than the timescale for SN explosions. Corbelli et al. (2017) used multiwavelength data, including Spitzer Space Telescope's 24 μm imaging, of the Local Group galaxy M33 to conclude that the embedded phase of star formation is short, ∼2 Myr. The main limitation of these studies is the use of low-resolution data. CO data usually subtend regions >50 pc in size, which suppresses the contrast at the small scales of stellar clusters (∼3 pc; Ryon et al. 2017; Brown & Gnedin 2021). Even in the favorable case of the nearby galaxy M33, the Spitzer MIPS/ 24 μm data subtends a spatial scale of 26 pc, much larger than a single stellar cluster. Spitzer imaging of the Magellanic Clouds provides spatial resolution ≈1 pc, thanks to the Clouds' small distances (Meixner et al. 2006; Gordon et al. 2011), suitable to investigating feedback. However, infrared studies of the Magellanic Clouds mostly concentrate on either individual sources or specific classes of objects (e.g., young stellar objects; Whitney et al. 2008; Sewiło et al. 2013). In one analysis of H II regions in the Clouds, Lawton et al. (2010) concluded that UV, Hα, and IR light track each other. Radio observations have been used to detect free–free emission from the gas ionized by newly formed massive stars embedded in their natal clouds (e.g., Kobulnicky & Johnson 1999; Johnson et al. 2001; Johnson & Kobulnicky 2003; Turner & Beck 2004; Johnson et al. 2009; Kepley et al. 2014), with some authors indicating an embedded timescale of ∼1 Myr (Johnson & Kobulnicky 2003). However, radio detection limits are usually too shallow to enable sampling of complete populations of stellar clusters (e.g., Reines et al. 2008).

In a pilot study, Messa et al. (2021) analyzed HST NUV-to-near-IR images of the nearby star-forming galaxy NGC 1313, isolating a population of stellar clusters that are dustier than those identified from NUV-optical images only. These authors find that about 40%–60% of the young stellar clusters (<6 Myr in age) are missed in UV-optically selected catalogs; in addition, they extend the timescale for emergence of the clusters from the natal cocoon from ≈2–3 Myr to ∼3–4 Myr, edging closer to the timescale of SN explosions. The main limitation of Messa et al.'s (2021) work is to still require that the sources are detected at visible wavelengths in order to constrain their ages and masses.

More recently, Linden et al. (2023) used near-IR imaging data from JWST to infer that about two-thirds of the stellar clusters younger than 4 Myr are missed by standard UV-optical observations in the relatively nearby luminous infrared galaxy

Table 1
Adopted Properties for NGC 4449

Parameter (Units)	Value	Reference[a]
Morphology	IBm	1
Distance (Mpc)	4.2	2
Recession velocity (km s^{-1})	207	3
Inclination (degrees)	68	4
$E(B-V)_{\text{MW}}$[b]	0.017	5
Stellar Mass ($M_\odot$)	1×10^9	6
SFR ($M_\odot$ yr^{-1})[c]	0.5	7
12+Log(O/H)[d]	8.26	8
Metallicity Gradient (dex/kpc)[d]	−0.055	9
[N II]/Hα	0.11	8

Notes. Data and references obtained from NED, the NASA/IPAC Extragalactic Database.
[a] 1—de Vaucouleurs et al. (1991); 2—(Tully et al. 2013, from TRGB); 3—Schneider et al. (1992); 4—Hunter et al. (2005); 5—Schlafly & Finkbeiner (2011); 6 —Calzetti et al. (2015b); 7—Lee et al. (2009); 8—Berg et al. (2012); 9—Pilyugin et al. (2015).
[b] Foreground Milky Way color excess.
[c] Star formation rate (SFR) from the dust attenuation-corrected UV luminosity.
[d] Central oxygen abundance and abundance gradient, respectively. The central oxygen abundance has an uncertainty of ± 0.09 (Berg et al. 2012).

VV114. Kim et al. (2023) used JWST mid-IR imaging, combined with Hα and CO imaging, of the nearby star-forming galaxy NGC 628 to infer that the embedded phase of star formation lasts about 5 Myr, during the first half of which dust obscuration is so high that the Hα emission is not detectable. In a complementary fashion, Whitmore et al. (2023) combined HST optical with JWST near- and mid-IR medium and broadband imaging of the galaxy NGC 1365 to conclude that massive ($M{\sim}10^6 M_\odot$) stellar clusters in this galaxy remain completely or partially obscured for about 4 ± 1 Myr. However, Linden et al. (2023), Kim et al. (2023), and Whitmore et al. (2023) do not have information on the infrared hydrogen recombination lines, which are key for constraining the ages of young stellar clusters when these are marginally detected or undetected at optical wavelengths. Clearly, more investigations are needed to obtain a census of the fraction of dust-embedded star formation in galaxies and address its implications for the efficacy of pre-SN feedback.

In this work, we attempt to mitigate earlier limitations with resolution and wavelength range by analyzing the compact source content of the nearby starburst dwarf galaxy NGC 4449 (Section 2) with broad- and narrowband NUV-to-near-IR imaging data from HST, covering the range 0.27–1.6 μm with angular resolution ∼0″.2. This angular resolution subtends a spatial scale of ∼4 pc at the distance of the galaxy, comparable to the size of stellar clusters (Ryon et al. 2017; Brown & Gnedin 2021). We also move away from standard optical-centered detections and require our sources to be undetected in the V band and bluer wavelengths, to attempt to secure truly dusty stellar clusters.

2. The Dwarf Starburst Galaxy NGC 4449

NGC 4449 is a nearby Magellanic irregular dwarf galaxy with ∼1/3 the stellar mass of the Large Magellanic Cloud (Table 1). Its star formation rate (SFR) is sufficiently high to place this galaxy about three times or more above the main-

Table 2
Imaging Data Sources

Instrument[a]	Filters[b]	Exposure Times[c]	Proposal ID[d]
(1)	(2)	(3)	(4)
WFC3/UVIS	F275W, F336W	2480, 2360	13364
ACS/WFC	F435W, F550M, F555W, F658N, F814W	7140, 1200, 4920, 2260, 4660	10522, 10585
WFC3/IR	F110W, F128N, F160W	1000, 2600, 1700	15330

Notes.

[a] WFC3/UVIS = Wide Field Camera 3 UV-Optical channel. ACS/WFC = Advanced Camera for Surveys Wide Field Channel. WFC3/IR = Wide Field Camera 3 Infrared channel.

[b] HST filter names.

[c] The total exposure time in each filter in seconds.

[d] Identification of the GO program that obtained the images: GO–13364 (LEGUS, Legacy ExtraGalactic UV Survey), PI: Calzetti; GO–10522, PI: Calzetti; GO–10585, PI: Aloisi; GO–15330, PI: Calzetti.

sequence of star formation for local galaxies (Whitaker et al. 2012; Cook et al. 2014), and thus qualify it as a starburst galaxy. The galaxy emits strongly at all wavelengths, including in the light of hydrogen recombination lines, in agreement with it rapidly forming stars at the present time. Star formation is centrally concentrated, with 90% located within 57% of R_{25}, as derived from dust attenuation-corrected UV images (e.g., Calzetti et al. 2018). For context, this corresponds to an SFR surface density, $\Sigma_{SFR} = 0.03\,M_\odot\,\mathrm{yr}^{-1}\,\mathrm{kpc}^{-2}$, about six times higher than the average in the Large Magellanic Cloud. The starburst in NGC 4449 has been triggered by either a minor merger or the interaction with another galaxy (Hunter et al. 1998; Lelli et al. 2014). The metal content is ∼40% of the solar value[9] (Berg et al. 2012), with a modest gradient (Table 1; Pilyugin et al. 2015). The slightly subsolar metallicity is consistent with the galaxy having a modest dust content: its IR/UV ratio indicates that only 40% of the light from young stars is absorbed by dust in this galaxy (Hao et al. 2011; Grasha et al. 2013).

3. Imaging Data and Processing

The HST observations used in this work were obtained from several programs, and cover the near-UV to near-IR range in 10 bands, listed in Table 2. The images obtained with the WFC3/IR camera are part of the program GO–15330, and include two continuum band filters (F110W and F160W) and one narrowband filter (F128N) centered on the Paβ(1.2818 μm) hydrogen recombination line emission. For each filter, the standard calibration pipeline CALWFC3 v. 3.5.2 was used to process individual frames into the final images, after correction for bias, dark, and flat-field. The UV and optical images were retrieved from the archive already processed through their respective instrumental pipelines. All images were aligned, mosaicked, and resampled to the smallest pixel scale, $0\rlap{.}{''}04\,\mathrm{px}^{-1}$, using DrizzlePac; alignment was performed on the Gaia DR2 reference frame. At the distance of NGC 4449, $0\rlap{.}{''}04$ subtends 0.81 pc. The final images are in units of e^-/s, and calibration to physical flux is performed by applying the image header keyword PHOTFLAM. Each filter's central wavelength and the limiting flux density reached in each image are listed in Table 3; the limiting flux density is calculated from the standard deviation of the eastern half of each image's field of view (FOV), where the galaxy's emission is fainter than the

average. The limiting flux is determined partly by the exposure time (i.e., the depth of the images) and partly by the density fluctuations in the galaxy's unresolved stellar field, since NGC 4449 is large enough to completely fill the FOV of the HST images. Within a small region, the limiting flux density can be higher or (slightly) lower than the average, depending on the local stellar density. The WFC3-IR camera has the smallest FOV among the instruments used, and determines the spatial coverage adopted in this analysis; it corresponds to the central, most active, $2.8 \times 2.4\,\mathrm{kpc}^2$ of the galaxy. This region encompasses 67% of the total SFR of the galaxy.

Emission-line images are obtained by subtracting the stellar continuum from the narrowband images. The stellar continuum for the F658N (Hα + [N II]) image is constructed from the interpolation between the F550M and the F814W, both tracers of stellar emission with only weak emission lines. The stellar continuum for the F128N (Paβ) image is obtained from the interpolation between the F110W and the F160W. Since the F110W also contains the Paβ line emission, the subtraction is performed iteratively; two iterations are sufficient for convergence to the final continuum-subtracted image. Both continuum-subtracted images are then multiplied by the respective filter widths (Table 3) and corrected for the filter transmission curve at the galaxy's redshift (Table 1), in order to derive line fluxes. The optical line is further corrected for the [N II] contribution, using the value of [N II]/Hα from Table 1. The final result is two emission-line images at Hα (λ0.6563 μm) and Paβ(λ1.2818 μm), respectively. A second near-IR line emission image is constructed at twice the pixel scale $(0\rlap{.}{''}08\,\mathrm{px}^{-1})$ of our default, since the point-spread function (PSF) of WFC3/IR images is about twice that of the optical images, $0\rlap{.}{''}19$ versus $0\rlap{.}{''}08$. This second Paβ line emission image is used to exclude artificial Paβ emission "sources" that may be produced by slight misalignments between the three near-IR images.

4. Source Selection

Our goal is to isolate sources that are emitting in the hydrogen recombination line and, thus, are possibly young stellar clusters, and are heavily attenuated by dust. Sources that are detected in Paβ, but are undetected in Hα would qualify as heavily attenuated, if they exist. We thus elect to visually inspect our images, searching for compact sources that are detected in F110W, Paβ, and F160W, are weakly detected in F814W, are marginally detected (signal-to-noise ratio, $S/N \lesssim 3$) in F658N, generally undetected or barely detected in the Hα line, and are

---

[9] We adopt a solar oxygen abundance of 12+Log(O/H) = 8.69; Asplund et al. (2009).

Table 3
Imaging Data Characteristics

HST Filter[a]	Pivot λ[b] (μm)	FWHM[b] (μm)	Standard Filter[b]	Limiting Flux Density[c] (erg s^{-1} cm^{-2} Å^{-1} px^{-1})	$\kappa(\lambda)$[d]
(1)	(2)	(3)	(4)	(5)	(6)
F275W	0.2710	0.04053	NUV	1.51×10^{-20}	6.285
F336W	0.3355	0.05116	U	8.87×10^{-21}	5.068
F435W	0.4329	0.06911	B	9.17×10^{-21}	4.186
F550M	0.5581	0.03845	Medium V	1.13×10^{-20}	3.045
F555W	0.5360	0.08478	V	9.23×10^{-21}	3.191
F658N	0.6584	0.00875	Hα+[N II]	1.47×10^{-20}	2.525
F814W	0.8048	0.15416	I	6.26×10^{-21}	1.831
F110W	1.1534	0.44300	J	1.91×10^{-21}	0.995
F128N	1.2832	0.01590	Paβ	1.82×10^{-21}	0.838
F160W	1.5369	0.26830	H	1.81×10^{-21}	0.627

Notes.

[a] WFC3/UVIS = Wide Field Camera 3 UV-Optical channel. ACS/WFC = Advanced Camera for Surveys Wide Field Channel. WFC3/IR = Wide Field Camera 3 Infrared channel.

[b] Filter names, pivot wavelength, FWHM (from the STScI Instrument Handbooks) and closest Standard Photometric System filter (Bessell 2005). For the narrowband filters, the main lines targeted are: Hα(0.6563 μm) and the [N II] (0.6548,0.6584 μm) doublet in F658N and Paβ(1.2818 μm) in F128N.

[c] The reported limiting flux densities are 1σ values averaged across the eastern half of the FOV of the images. The pixel size is 0''04.

[d] The values of the extinction curve: $\kappa(\lambda) = A(V)/E(B - V)$ adopted in this work (from Fitzpatrick et al. 2019) to correct fluxes for the foreground Milky Way dust extinction.

undetected in any filter bluer than F658N. When evaluating the detection level of the line emission from the sources, we consider that it may be nested amid diffuse emission.

Qualitatively, we already know what kind of sources we are likely to identify. For a line-emitting source with about $1/2$ solar metallicity, Hα/Paβ = 17.6 (Osterbrock & Ferland 2006; Calzetti et al. 2007). If we require that Paβ is detected at least at the 3σ level and Hα is undetected (i.e., $\lesssim 1\sigma$), we constrain our sources to have at least a color excess $E(B - V) \gtrsim 2.1$ mag ($A(V) \gtrsim 6.5$ mag). These values translate to a minimum suppression of a factor ~ 135 for Hα and ~ 5 for Paβ. The actual minimum value of $E(B - V)$ will be higher than 2.1 mag, as our estimate does not include the contribution of the stellar continuum to the narrowband filters. The calculation assumes a foreground dust geometry and takes into account that the F658N image has twice the angular resolution of the F128N image and is eight times less deep (Table 3).

We use the Paβ line emission images at both pixel scales: 0''08 and 0''04 px^{-1} to ensure that our detections do not suffer from biases due to small misalignments among the images that could create spurious "emission" sources. We further inspect all candidate sources for potential artifacts, such as saturation in F110W and F160W, which would create an artificially low stellar continuum image under the F128N filter resulting in "emission-line sources." We test the effects of continuum undersubtraction, which would also artificially create "emission-line sources" in the narrowband filter, by multiplying the two IR broadband images by increasing factors up to $\sim 15\%$; this value represents a hard upper limit to the combined uncertainties of the continuum interpolation and the absolute photometric calibration of the WFC3 bands.[10] The effect of this operation on the Paβ image is to remove the diffuse emission, creating obvious oversubtracted images, and depressing the compact source line emission, but without removing it. Thus, both saturation and undersubtraction are excluded as problems for our sources. We finally exclude any source that

has another source within an aperture of 5 px (0''20) radius in the F814W and shorter wavelength images; this is to ensure that no contamination from neighboring sources (including their wings) affects the photometry in the lower-resolution WFC3/IR images, which have PSF FWHM = 0''19 ($\sim$5 px).

After all selections above are implemented, the original sample of $\sim$60 candidates is reduced to 34 sources, listed in Table 5. The location of the 34 sources is shown in Figure 1. An example of the sources in our sample is shown in Figure 2, while two examples of "discarded" sources are shown in Figure 3. The breakdown of reasons for discarding sources is as follows: about two-thirds are rejected because the Paβ line emission appears misaligned with the continuum images, which may potentially result in undersubtraction of the narrowband F128N image;[11] of the remaining one-third discarded sources, about half are rejected because they are detected in F555W and half because of nearby contaminating sources.

A comparison with the distribution of the dust emission traced by the Spitzer Space Telescope's 8 μm image shows that all 34 retained sources are in areas of the galaxy where dust emission is present. The low resolution of the Spitzer images does not allow us to obtain deeper insights, except to estimate that even the most "dust faint" among our sources resides in an area with 8 μm dust emission detected at least to the 9σ level (Figure 2). The 8 μm dust image for NGC 4449 is derived from the IRAC 8 μm mosaic, after subtraction of the stellar continuum using the IRAC 3.6 μm image (see description and details in Calzetti et al. 2018). The coincidence of our sources with 8 μm dust-emitting regions in the galaxy further reinforces that our sources are unlikely to be image artifacts. The identified sources are extremely compact with several unresolved sources, as measured in the F814W filter; the most

---

[10] https://hst-docs.stsci.edu/wfc3dhb/chapter-7-wfc3-ir-sources-of-error/7-11-ir-photometry-errors

[11] These sources could have misaligned line-continuum simply because the gas is physically displaced from the centroid of the stellar continuum and, thus, be true line-emitting sources. However, the low resolution of the WFC3/IR images does not enable us to assess this scenario, and the sources are conservatively discarded.
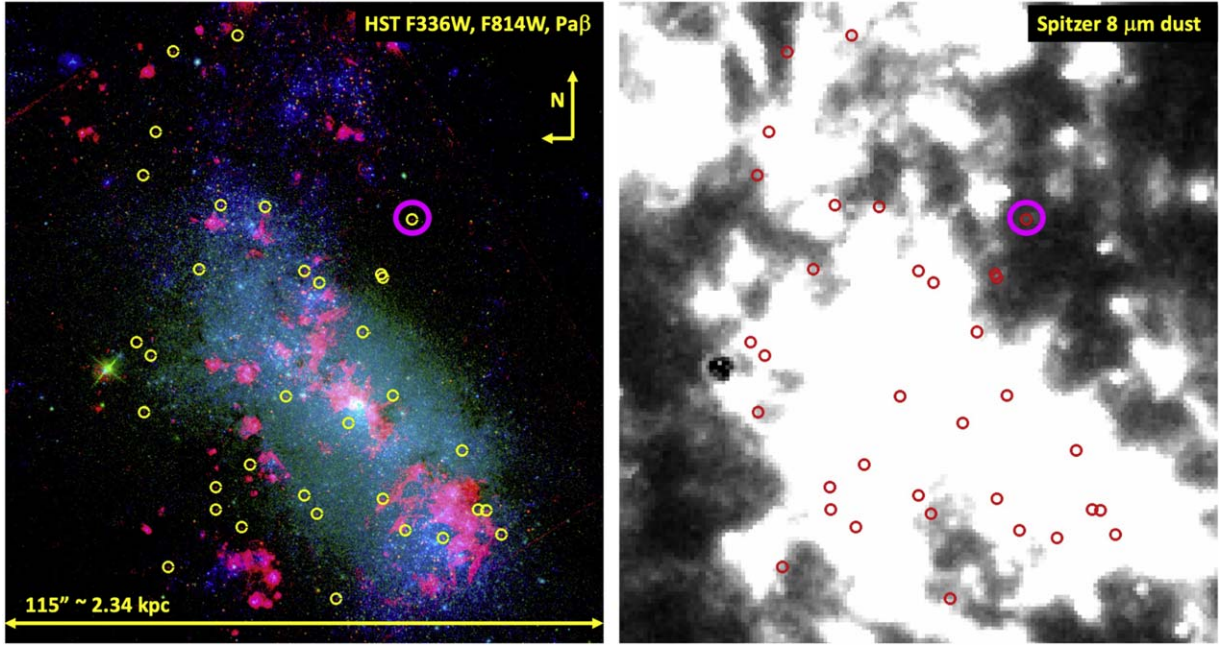
Figure 1. Location of the 34 Paβ emitting sources shown on a three-color composite (left; blue = F336W, green = F814W, red = Paβ emission) and on a 8 μm dust image (right) of NGC 4449. The three-color composite uses the HST images discussed in this paper; the 8 μm dust image is obtained from the Spitzer IRAC 8 μm image after removal of the stellar continuum by subtracting the IRAC 3.6 μm image (e.g., Calzetti et al. 2018). The location of the sources is marked by yellow (left) and red (right) circles, respectively. All identified sources are in correspondence of strong dust emission from the galaxy. The magenta circle identifies the source shown in detail in Figure 2. North is up, east is left.
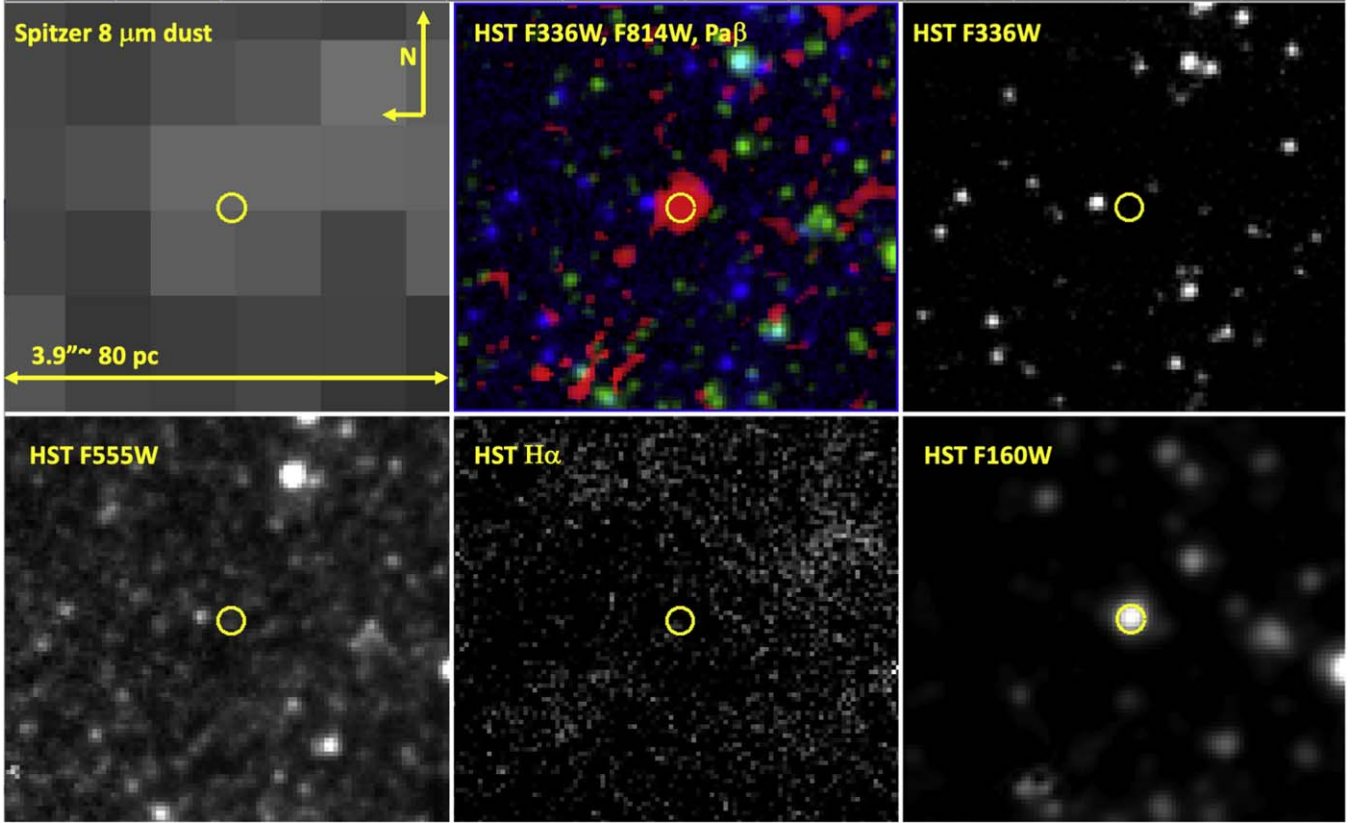

Figure 2. The location of source #29 is indicated by a yellow circle and shown at a range of wavelengths. The yellow circle has a radius of 3 px (0″12), which is the size of our photometric apertures. This is the cluster marked with a magenta circle in Figure 1. Despite being located in a relatively dust-faint area of the galaxy, its 8 μm dust emission is still detected at 9σ. The cutouts show (from top-left to bottom-right): the Spitzer 8 μm dust emission, the HST three-color composite as in the previous figure, and single-band HST emission in the light of F336W (U), F555W (V), Hα, and F160W (H). Like all sources considered in the present analysis, this source is only detected in the I band (F814W) and at longer wavelengths and marginally detected in F658N, but is undetected at shorter wavelengths. In particular, while the Paβ emission is strong, the Hα emission is generally not or only weakly detected above the diffuse background.
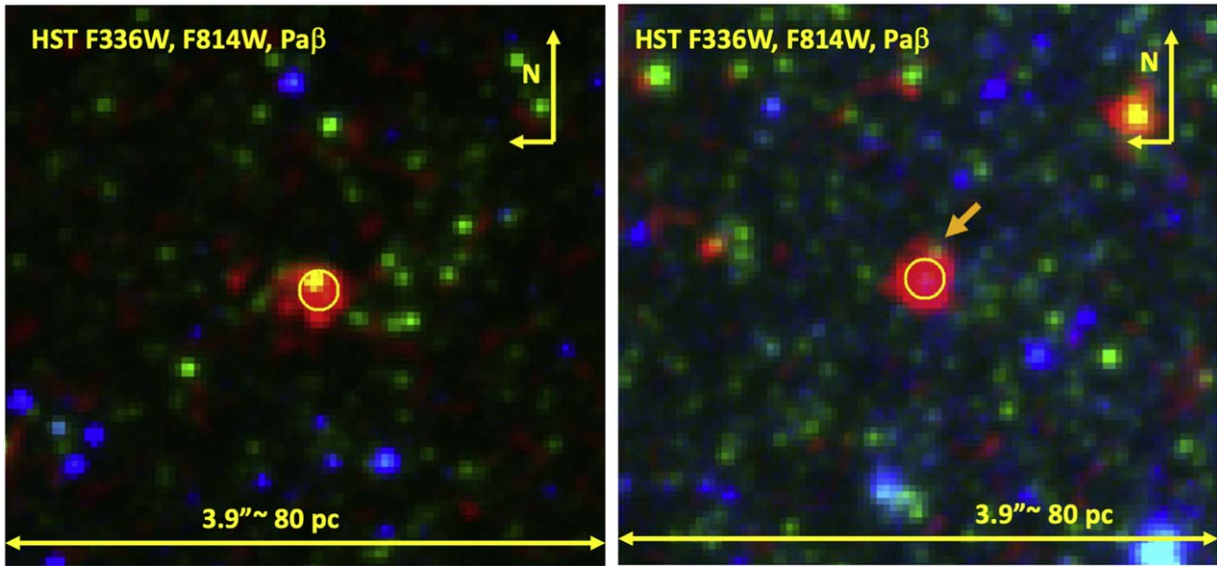
Figure 3. Two examples of discarded sources, marked by a yellow circle. Like in Figure 2, the yellow circle has a radius of 3 px (0″12). The source to the left was discarded because the continuum source is slightly misaligned with the center of the line emission, raising the suspicion that the observed line emission may be the result of undersubtraction of the underlying stellar continuum due to potential offsets between the narrowband and broadband filters. The source to the right was discarded because of the presence of an adjacent optically emitting source (top-right of the yellow circle, indicated by an orange arrow), which may affect photometry in the IR bands. The HST three-color composite is as in the previous figure.

frequent (deconvolved) size is ≈ 1 pc ($\approx 0''05$), with a range $<0.5-5$ pc. The sources are consistent with point sources in the near-IR bands, including in the line emission, although this is to be expected, as the near-IR images have lower angular resolution than the I-band image. If the sources are stellar clusters, they are extremely compact, similar to the result by Messa et al. (2021) for NGC 1313.

5. Photometry

Photometry is performed in circular apertures on all sources in all bands. The apertures are chosen with 3 pxels radius ($0''12 = 2.44$ pc) on the plane of the sky to ensure that all photometry, and especially the upper limits (all bands shortward of F658N), are not affected by the presence of neighboring contaminants, like, e.g., in the case of the discarded source in Figure 3, right. The photometry is background-subtracted using a background annulus 5 px in radius and 2 px in thickness. Aperture corrections are applied to the measurements to account for the flux outside of the 3 px aperture. As the sources are consistent with point or extremely compact sources (see previous section), we use isolated stellar sources in the images to measure the curves of growth and the aperture corrections. We derive the following aperture corrections: 1.60 ± 0.04 for F814W, 2.54 ± 0.05 for F110W, 2.65 ± 0.05 for F128N, and 2.91 ± 0.04 for F160W. We apply the F814W aperture corrections also to the F658N measurements and the upper limits at bluer bands, based on the results of Messa et al. (2021) who determine that differences in aperture corrections between HST UV and I band are $\lesssim 10\%$. Finally, all photometry is corrected for the MW foreground extinction, $E(B - V) = 0.017$ (Table 1). Uncertainties in the photometry are the geometric combination of photon noise, uncertainty in the aperture correction, and the standard deviation of the background measurement (which also includes instrumental uncertainties). The final photometry is listed in Table 5, together with the luminosity and equivalent width (EW) of Paβ.

Our 2.44 pc (3 px) aperture radius on the plane of the sky corresponds to an ellipse of 2.44×6.51 pc^2 on the plane of the galaxy, based on its inclination (Table 1); this is equivalent to a circular aperture (by area) of 3.5 pc radius. Ryon et al. (2017) found that the peak of the distribution of effective radii of stellar clusters in two galaxies of the LEGUS sample, which is a sample of galaxies within $\sim$12 Mpc (Calzetti et al. 2015b), is at 2–3 pc. Brown & Gnedin (2021) found, for the full LEGUS sample of galaxies, a shallow correlation between cluster effective radii and stellar mass: clusters with mass $\sim 10^4 M_\odot$ have effective radii $\sim$2.6 pc, which rescales according to the relation $R_{\rm eff} \propto M^{0.24}$ for different masses. Thus, if our sources are stellar clusters, the photometric aperture we have chosen is a reasonable compromise between capturing the clusters' emission and minimizing contamination from neighboring sources.

6. Models and Fitting Approach

We compare the photometry of the 34 sources measured above (Section 5) with models, in order to derive physical properties: age, mass, and extinction, under the assumption that the presence of the hydrogen recombination line emission is likely tracking young stellar clusters. We generate synthetic photometry from the Yggdrasil spectral energy distribution (SED) models (Zackrisson et al. 2011) combined with dust attenuation/extinction recipes, following the same procedure outlined in Calzetti et al. (2015a), Adamo et al. (2017), Messa et al. (2021), and Calzetti et al. (2021) and briefly summarized here.

Yggdrasil uses the Starburst99 (Leitherer et al. 1999) spectral synthesis models as an input for CLOUDY (Ferland et al. 2013), to produce single stellar population (SSP) models that include, in addition to a stellar and nebular continuum (a standard output of Starburst99), also nebular emission lines. The SSP models from Starburst99 are generated using instantaneous star formation, with a Kroupa (2001) initial mass function (IMF) in the range 0.1–120 $M_\odot$ and metallicity $Z = 0.008$ ($\sim$40% solar), which is the closest value to the

measured oxygen abundance of NGC 4449 and for which models are available. The models are produced using both the Padova with asymptotic giant branch (AGB) treatment and the Geneva tracks (Meynet et al. 1994; Girardi et al. 2000; Vázquez & Leitherer 2005). From the Yggdrasil suite, we adopt the models with a 0.5 covering factor for the ionized gas, meaning that only 50% of the Lyman continuum photons produced by the stellar cluster ionize the gas. Although we do not have a handle on the actual gas covering factor of our sources, it is reasonable to expect that not all ionizing photons are available to ionize the surrounding gas: at the large extinctions of our sources, a significant portion of the ionizing photons is likely to be absorbed directly by the dust in which the sources are embedded (Dopita et al. 2003). Models are generated with ages between 1 Myr and 14 Gyr; however, we are interested in the youngest (ionizing) ages, <10 Myr, for which the models are generated in 1 Myr steps. We determine a posteriori that the sources under consideration are massive, with median $M \sim 5600\,M_\odot$ and a minimum mass of $\sim 3000\,M_\odot$. This, coupled with the fact that all of our sources are detected in hydrogen recombination line emission, implies that we expect minimal impact from stochastic sampling of the IMF (Cerviño et al. 2002), and use deterministic models, i.e., full sampling of the stellar IMF, for the derivation of the physical parameters.

The SSP SEDs are then attenuated with: a starburst attenuation curve (Calzetti et al. 2000) and an LMC extinction curve (as parameterized by Fitzpatrick 1999). We adopt a foreground dust geometry (Calzetti 2001) of the form:

$$F(\lambda)_{\mathrm{final}} = F(\lambda)_{\mathrm{model}} 10^{[-0.4E(B-V)\kappa(\lambda)]}, \qquad (1)$$

where $E(B-V)$ is the color excess and $\kappa(\lambda)$ is the attenuation/extinction curve. No other extinction curve beyond the LMC is considered here, because our sources are undetected at V and blueward, and functional shape differences among extinction curves are only found below the V band (Gordon et al. 2003). For the LMC extinction curve, both cases of equal and differential attenuation for the nebular gas and stellar continuum are considered; for the differential attenuation, we assume that the stellar continuum is subject to about half the attenuation of the nebular gas (Calzetti et al. 1994; Kreckel et al. 2013). For the starburst attenuation curve, the dust geometry, including the differential attenuation, is "built-in" into the functional form of the curve. In summary, we generate models with three types of extinction/attenuation: LMC, LMC with differential attenuation between ionized gas and stellar emission, and starburst. We generate the models in the color excess range $E(B-V) = 0 - 5$ mag, with step 0.02.

We only consider foreground dust attenuation/extinction because more complex geometries, including mixed dust/star/gas geometries, maximize total attenuation while minimizing differential attenuation (Gordon et al. 1997; Calzetti 2001). For instance, in the extreme case of homogeneously mixed dust and stars/gas with large dust column density, the net effect is to drastically dim the source while maintaining a blue overall SED (Calzetti et al. 1994, 2015a). In our case, we are trying to select geometries that maximize differential attenuation, so to abate the emission in the blue bands while keeping the I and near-IR bands above their respective detection thresholds.

The dust-attenuated model SEDs are convolved with the transmission curve of the filters plus the HST optics to produce synthetic photometry for all six model combinations (two tracks and three extinction/attenuation recipes). The synthetic photometry is then compared with the measured photometry using χ^2-minimization, taking into account the measurement uncertainties, to obtain the distribution of solutions and the reduced χ^2 value for each source. We finally plot the distribution of solutions within the 90% significance level for the appropriate number of degrees of freedom, and select the best values and the 68% (1σ) uncertainty for the parameters of each region based on the shape of the reduced χ^2 probability distribution.

The presence of emission in the Paβ line already enables us to break some degeneracies in the fits, since our sources are likely to have young ages. Thus, we do not expect the usual age–extinction degeneracy between "dusty and young" and "dust-free and old" often found in SED fits (Whitmore et al. 2020).

Although we measure photometry in 10 separate bands, we have upper limits for the five bluest ones. The reddest upper limit, the luminosity density in F550M, provides the bluest useful constraint to the SED fits, meaning that we are effectively using six data points for the fits; thus, we have $3°$ of freedom. Below the F550M upper limit, we do not consider deviations between the remaining upper limits and the fits as being meaningful. We include the narrowband F658N and F128N filters in the fits, although gas emission can have a different spatial distribution from that of the stars (Calzetti et al. 2015a). We do this for two reasons: (1) we have a limited number of measurements for our SEDs (excluding upper limits), and (2) our sources are pointlike at all bands where they can be measured, suggesting that the sources are confined by the surrounding medium and the ionized gas is cospatial with the stars.

7. Results

The combination of Geneva models with the LMC extinction curve yields the lowest χ^2_{red} overall across the 34 regions. Examples of the best-fit SEDs are shown in Figures 4 and 5 for a selection of χ^2_{red} values. The best-fit age, mass, and color excess for each source, with their χ^2_{red} values, are listed in Table 4. We define as "acceptable" a fit with $\chi^2_{\mathrm{red}} \leqslant 6$; this is an arbitrary value chosen on the basis of visual inspection of the SED fits, resulting in 23 sources with acceptable fits. The choice of $\chi^2_{\mathrm{red}} \leqslant 6$ as cutoff has modest impact on our conclusions; choosing $\chi^2_{\mathrm{red}} \leqslant 4$ would still yield 22 sources with acceptable fits (Table 4). The remaining sources range in χ^2_{red} value from bad to catastrophically bad; these sources will be indicated as "low significance," with different symbols from the acceptable ones in all Figures that follow. The case of the worst χ^2_{red} is shown in the right panel of Figure 5. The best-fit ages are concentrated around 5–6 Myr, while the masses span the ~ 3000–$25,000\,M_\odot$ range, with a median value of $5600\,M_\odot$ (Figure 6, left panel). These mass values support our use of deterministic models for deriving the physical parameters of the sources. The color excess $E(B-V)$ is systematically high, $\gtrsim 2$ mag, as expected from earlier considerations based on Hα and Paβ selection criteria (Figure 6, right). The measured EW(Paβ) as well as the $J - H$ colors agree with the model expectations; in particular, the observed $J - H$ colors are
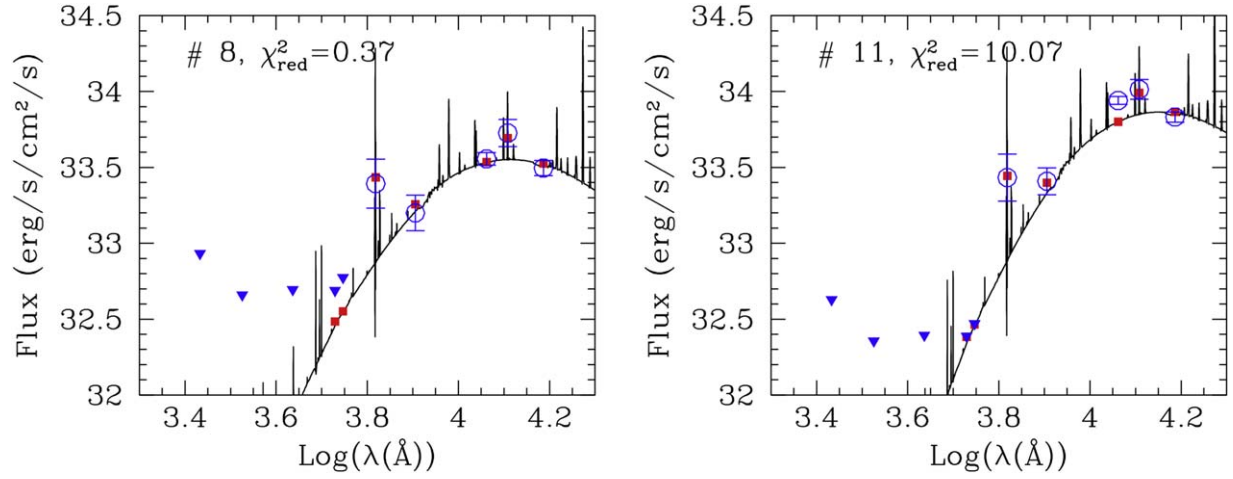
Figure 4. The measured and best-fit photometry and model spectra for two sources, showing two very different cases: an excellent goodness-of-fit ($\chi^2_{red} < 1$) and a low-significance one ($\chi^2_{red} > 10$). The measurements (circles with 1σ error bars) and upper limits (downward triangles) are shown in blue. Best-fit photometry is shown as red squares, and the best-fit spectrum is shown as a black line. The source ID is listed in each panel, and corresponds to the IDs listed in both Tables 5 and 4.
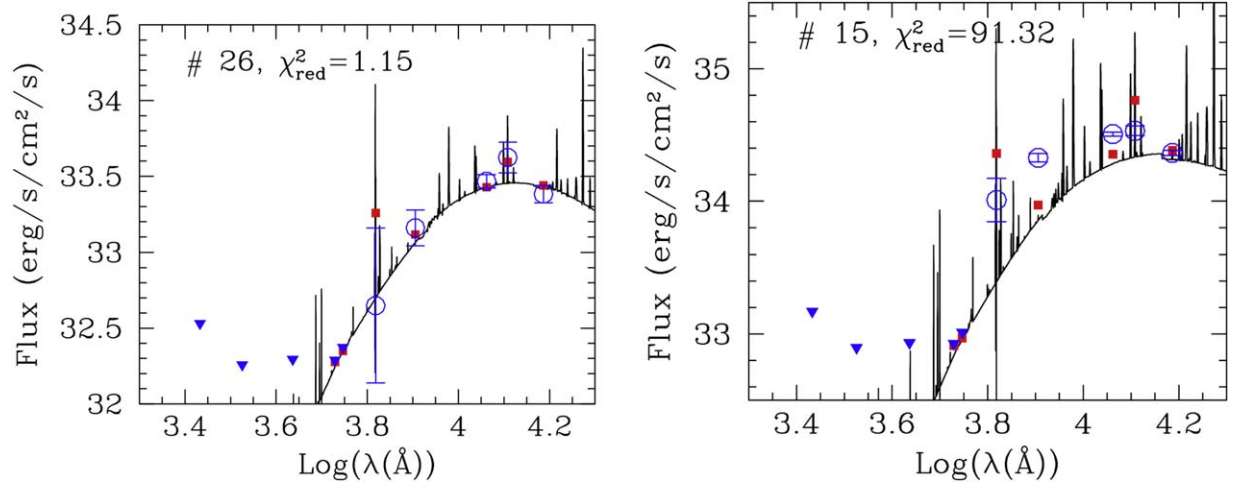

Figure 5. Two additional examples of observed photometry and best fit for our sources, including the case of the worse χ^2_{red} in our sample (right panel). Symbols and lines are as in Figure 4.

consistent with stellar populations attenuated by large values of $E(B - V)$ (Figure 7).

Using the Padova+AGB tracks instead of the Geneva ones yields slightly worse χ^2_{red} values, between a few percent to a factor ~1.5, with a median fraction ~20% worse. However, the general picture does not change: ages are still around 5–6 Myr, extinctions are high, and masses are large, between a few percent and a factor ~2 larger than for the Geneva tracks. Figure 8 illustrates some of these results.

The combination of Geneva models with the other two dust attenuation prescriptions considered in this work, i.e., differential-LMC and starburst, yields slightly worse and significantly worse χ^2_{red} values for the fits, respectively. The χ^2_{red} resulting from using the starburst curve is at least a factor of 2–3 worse than using the LMC curve, and we drop this option from further consideration. We discuss the differential-LMC case in greater detail, as the χ^2_{red} discrepancies with the LMC case are relatively small. The masses and ages resulting from the differential-LMC case are displayed in Figure 9 in comparison to our default case of the LMC extinction, to highlight similarities and differences. The clearest difference between the two attenuation approaches is that the fits with the

differential-LMC extinction yield a wider range of ages for the sources, ~3–8 Myr. In particular we now find 11 sources, i.e., half of the high-significance ones, with ages $\leqslant 4$ Myr, as opposed to none with the standard LMC extinction. However, in most cases, the values of the χ^2_{red} for the differential-LMC extinction are worse than those for the standard LMC extinction (Figure 9, right); only for six sources (three with age 3 Myr and three with age 4 Myr) the goodness-of-fit improves in the case of the differential-LMC extinction. Furthermore, the best-fit $E(B - V)$ values are all larger than 2.5 mag for the differential-LMC extinction; thus, they do not change the overall scenario that these are extremely dust-reddened sources.

One important limitation of our models is the absence of pre-main-sequence stars, which are expected to be present at these young ages and contribute to the near-IR continuum emission. Greissl et al. (2010) explicitly considered the contribution of pre-main-sequence stars in their modeling of the near-IR data of a young stellar cluster in the Antennae galaxy. They conclude that the contribution from these unevolved stars is already small at 3 Myr, and rapidly decreases for increasing

Table 4
Physical Properties of the Sources

ID[1]	Age_{SED} Myr	$E(B-V)_{SED}$ mag	$Log(Mass_{SED})$ $M_\odot$	χ^2_{red}
1	$5.^{+1.}_{-0.}$	$2.98^{+0.02}_{-0.06}$	$4.09^{+0.02}_{-0.15}$	3.41
2	$4.^{+0.}_{-0.}$	$3.10^{+0.04}_{-0.02}$	$4.11^{+0.01}_{-0.03}$	14.00
3	$6.^{+0.}_{-1.}$	$3.38^{+0.08}_{-0.00}$	$4.20^{+0.14}_{-0.01}$	11.39
4	$6.^{+2.}_{-1.}$	$3.02^{+0.52}_{-0.36}$	$3.72^{+0.27}_{-0.38}$	0.39
5	$4.^{+2.}_{-0.}$	$3.22^{+0.06}_{-0.20}$	$4.38^{+0.02}_{-0.41}$	15.48
6	$6.^{+0.}_{-1.}$	$2.82^{+0.10}_{-0.00}$	$3.98^{+0.14}_{-0.03}$	3.26
7	$6.^{+1.}_{-1.}$	$2.36^{+0.16}_{-0.20}$	$3.80^{+0.14}_{-0.24}$	1.47
8	$5.^{+1.}_{-0.}$	$2.36^{+0.32}_{-0.24}$	$3.73^{+0.10}_{-0.21}$	0.37
9	$6.^{+1.}_{-1.}$	$2.72^{+0.44}_{-0.22}$	$3.78^{+0.19}_{-0.26}$	0.97
10	$6.^{+0.}_{-1.}$	$2.92^{+0.22}_{-0.04}$	$3.99^{+0.17}_{-0.01}$	2.69
11	$5.^{+0.}_{-0.}$	$2.80^{+0.04}_{-0.00}$	$4.17^{+0.01}_{-0.01}$	10.07
12	$6.^{+0.}_{-0.}$	$2.68^{+0.10}_{-0.00}$	$4.03^{+0.14}_{-0.01}$	10.21
13	$5.^{+1000}_{-0.}$	$4.04^{+0.62}_{-1.74}$	$4.18^{+0.22}_{-0.81}$	1.12
14	$6.^{+1.}_{-1.}$	$2.52^{+0.28}_{-0.40}$	$4.14^{+0.18}_{-0.27}$	3.45
15	$4.^{+0.}_{-0.}$	$2.94^{+0.02}_{-0.02}$	$4.96^{+0.00}_{-0.01}$	91.32
16	$6.^{+1.}_{-1.}$	$3.28^{+0.30}_{-0.62}$	$4.27^{+0.18}_{-0.35}$	2.72
17	$4.^{+2.}_{-0.}$	$2.78^{+0.14}_{-0.22}$	$4.07^{+0.03}_{-0.41}$	10.19
18	$6.^{+1.}_{-1.}$	$2.32^{+0.20}_{-0.22}$	$3.71^{+0.17}_{-0.24}$	1.71
19	$6.^{+0.}_{-1.}$	$2.20^{+0.08}_{-0.04}$	$3.58^{+0.14}_{-0.04}$	8.02
20	$6.^{+2.}_{-1.}$	$2.52^{+0.46}_{-0.48}$	$3.67^{+0.25}_{-0.41}$	0.64
21	$6.^{+0.}_{-1.}$	$3.02^{+0.24}_{-0.04}$	$3.82^{+0.42}_{-0.04}$	10.76
22	$6.^{+1.}_{-1.}$	$2.56^{+0.40}_{-0.22}$	$3.61^{+0.21}_{-0.24}$	2.66
23	$2.^{+2.}_{-0.}$	$3.00^{+0.08}_{-0.02}$	$4.10^{+0.00}_{-0.02}$	60.38
24	$5.^{+2.}_{-1.}$	$2.72^{+0.30}_{-0.28}$	$3.54^{+0.31}_{-0.36}$	2.69
25	$6.^{+0.}_{-1.}$	$2.80^{+0.10}_{-0.00}$	$4.02^{+0.14}_{-0.01}$	16.19
26	$5.^{+2.}_{-0.}$	$2.48^{+0.22}_{-0.30}$	$3.67^{+0.05}_{-0.38}$	1.15
27	$6.^{+0.}_{-1.}$	$2.90^{+0.12}_{-0.02}$	$3.79^{+0.15}_{-0.02}$	4.55
28	$5.^{+2.}_{-1.}$	$3.02^{+0.88}_{-0.86}$	$3.55^{+0.43}_{-0.67}$	1.01
29	$6.^{+1.}_{-1.}$	$3.08^{+0.30}_{-0.22}$	$3.91^{+0.18}_{-0.24}$	2.43
30	$5.^{+1.}_{-0.}$	$3.70^{+0.40}_{-0.40}$	$4.37^{+0.13}_{-0.23}$	1.14
31	$5.^{+1.}_{-0.}$	$2.86^{+0.22}_{-0.06}$	$3.97^{+0.14}_{-0.06}$	1.51
32	$5.^{+2.}_{-1.}$	$2.64^{+0.64}_{-0.22}$	$3.60^{+0.39}_{-0.36}$	1.20
33	$6.^{+1.}_{-1.}$	$2.32^{+0.44}_{-0.28}$	$3.47^{+0.24}_{-0.29}$	0.52
34	$6.^{+1.}_{-2.}$	$2.78^{+0.24}_{-0.24}$	$3.45^{+0.40}_{-0.26}$	1.89

Note. Age (Myr), color excess $E(B - V)$ (mag), logarithm of the stellar mass ($M_\odot$), and reduced χ^2 from the SED fit of the photometry in Table 5 for the 34 sources in our sample.

(This table is available in machine-readable form.)

age. We thus conclude that the contribution of pre-main-sequence stars to our results is negligible.

For completeness, we also attempt SED fits using synthetic photometry of red supergiants (RSGs). RSGs' luminosities in the Large Magellanic Cloud, which has roughly the metallicity of NGC 4449, can be as bright as 10^{34} erg s^{-1} Å^{-1} in the J and H bands, with $Log[f(J)/f(H)] \sim 0.1$–0.12 (Oestreicher et al. 1997; Davies et al. 2013). Both luminosities and colors are in the range of what we observe for our sources (Table 5 and Figure 7), although RSGs do not have line emission at 1.28 μm. We use the model spectra of Lançon et al. (2007) with a fiducial temperature of 3500 K, which matches the typical temperatures of LMC RSGs (Davies et al. 2013). The model spectra are provided at three gravity values (Lançon et al. 2007), and we use all three to maximize our probability of matching the observed SEDs. We find that the SED fits using these models yield >50% worse goodness-of-fit than the fits

using the SSP models, without solving the "too much extinction" problem: the typical source, if they are RSGs, needs to be behind a dust screen with $E(B - V) > 1$ mag in order to match our observations.

In summary, the Geneva tracks with the LMC extinction curve yield the best results in terms of goodness-of-fit as measured from the χ^2_{red}: the sources have ages ~ 5–6 Myr, masses with median value 5600 $M_\odot$, and foreground extinctions $E(B - V) > 2$ mag. About a half-dozen sources are better fit with the differential-LMC extinction, and have ages that are ~ 3–4 Myr, masses $> 10^4\, M_\odot$, and extinctions $E(B - V) > 2.6$ mag. As these sources represent only 25% of our high-significance sample, we will only use the results from the standard LMC extinction fit, listed in Table 4, as our fiducial results for the reminder of the paper.

8. Discussion

8.1. What Are These Sources?

The ages and masses from SED fits and the presence of hydrogen recombination line emission make our sources consistent with being young stellar clusters, younger than ~ 7–8 Myr. The requirement that the Paβ emission be detected with S/N $\gtrsim 3$ places a constraint on its EW, and thus on the maximum age of the sources: the minimum EW ~ 25 Å translates into a maximum age of about 6–7 Myr (Leitherer et al. 1999). For reference, beyond 7 Myr, the ionized gas emission is between >30 (Padova+AGB) and >50 (Geneva) times fainter than at 3 Myr.

The existing studies on the stellar cluster population of NGC 4449 center on optically detectable sources (Whitmore et al. 2020), and are thus complementary to our selection of optically faint sources. We compare our sources with the optically bright clusters in a later subsection. Sokal et al. (2015) identify a partially embedded, Wolf–Rayet stellar cluster in the galaxy; the presence of Wolf–Rayet features gives this cluster a minimum age of 3 Myr and indicates that stellar winds are active in NGC 4449. This cluster would provide an important comparison for our sources, but it falls outside the FOV of our WFC3/IR images. The closest study to ours is the one by Reines et al. (2008), where the authors focused on radio-selected sources.

Reines et al. (2008) identified 39 compact sources in their Very Large Array (VLA) observations at 1.3, 3.6, and 6 cm of NGC 4449. Of these 39 sources, 13 were classified as thermal or "likely thermal," four are mixed, and the remaining ones are either nonthermal or uncertain. The 39 sources are shown in Figure 10, left panel, with white circles for the thermal/likely thermal/mixed sources and yellow circles for the other sources. Our sources are located in correspondence of the red circles on the same figure. The radio sources are clearly separated from the dust-buried sources in our sample. They are generally located in areas of intense Hα emission, while the dust-buried sources are, by design, located at the edges of or away from the brightest line emission regions.

Reines et al. (2008) modeled the 13 thermal and likely thermal sources in their sample using multiwavelength data from the UV to the radio. The sources have ages in the range ~ 2.5–5.5 Myr with a median of 3.6 Myr and masses in the range $\sim (6$–51$) \times 10^3\, M_\odot$, with a median of $16 \times 10^3\, M_\odot$, after rescaling to our preferred distance (cyan data points in Figure 6). Their sources on average are a factor ~ 1.5 younger and ~ 3 more massive than ours. These authors observe a
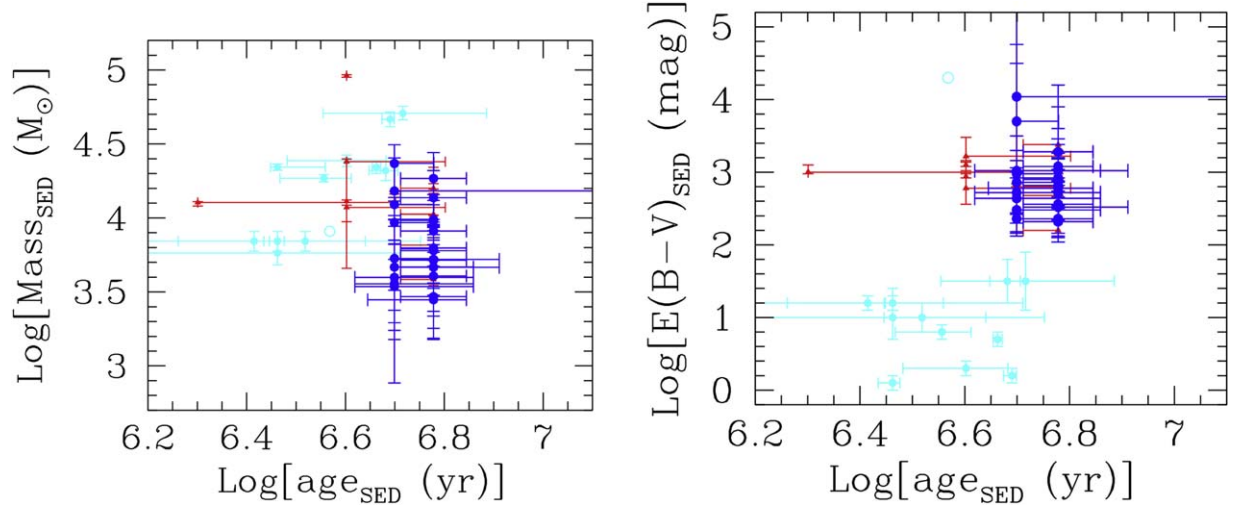
Figure 6. Left: the stellar mass as a function of the age derived from the SED fits, with 1σ uncertainties. Blue points indicate sources with $\chi^2_{red} \leqslant 6$ from the SED fits (see list in Table 4), while red points are for sources with larger values of χ^2_{red}. A total of 23 sources, two-thirds of the final sample, have good SED fits according to this criterion. The cyan points show the location, with uncertainties, on this plot of the radio sources from Reines et al. (2008), after rescaling to our preferred distance for NGC 4449; the empty cyan circle marks the upper limit in the Reines et al. (2008) sample. Right: the color excess, $E(B - V)$, as a function of age derived from the SED fits. Symbols and error bars are as in the left panel.
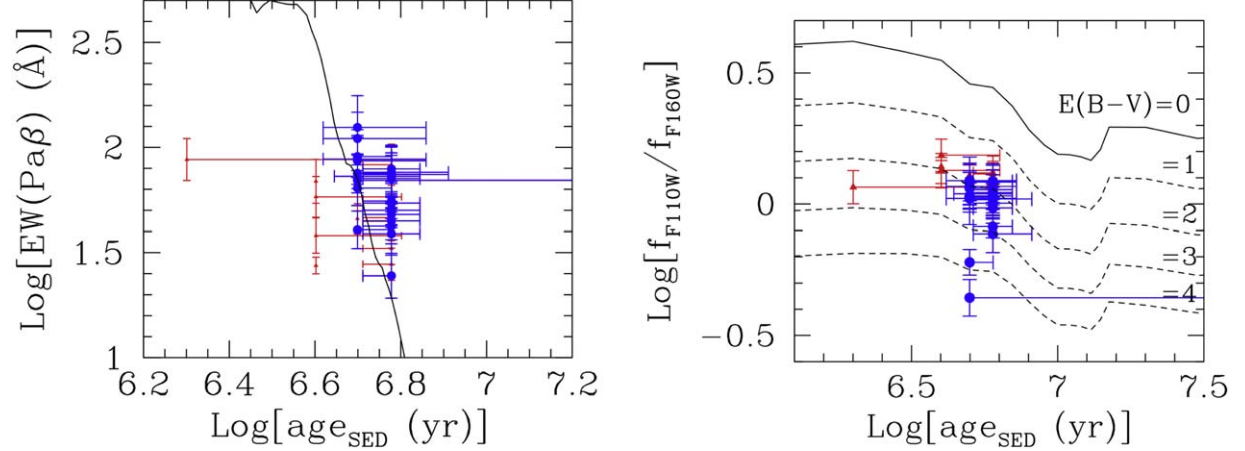

Figure 7. Left: the EW(Paβ) as a function of the age derived from the SED fits, with 1σ uncertainties. The data are compared with the models from Starburst99 for Geneva tracks, showing that the SED ages are consistent with the measured line EW. Right: the observed broadband IR colors $J - H$ as a function of the age from the SED fit; symbols are as in the previous panel. Yggdrasil models with Geneva tracks for the colors are shown for increasing values of the color excess $E(B - V)$, showing that the data are consistent with large values of the color excess, in agreement with results from the fits. It should be noted that this comparison is somewhat circular, since the colors are used to derive the ages and color excesses. Symbols are as in Figure 6.
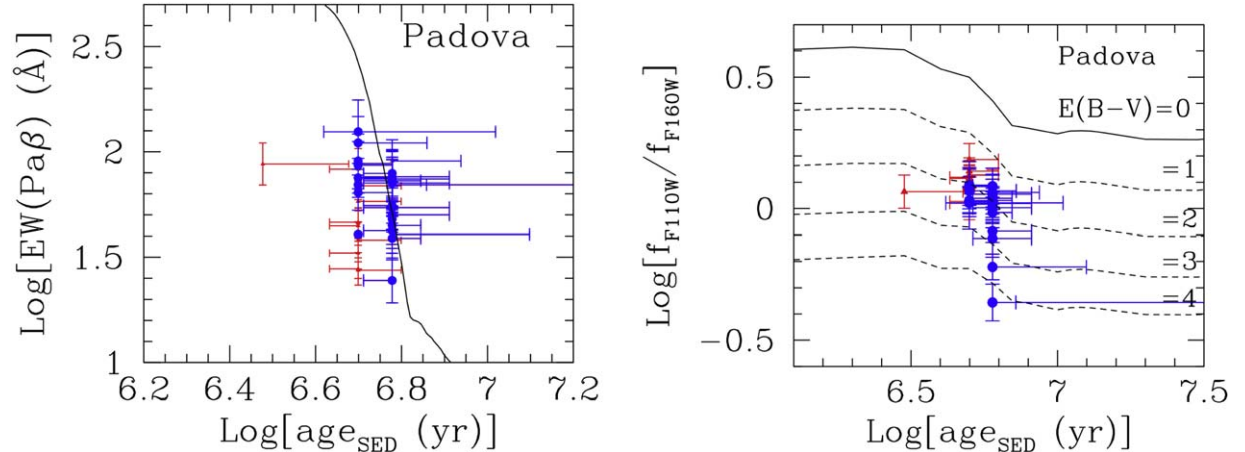

Figure 8. The same as Figure 7, but using the Padova+AGB tracks instead of the Geneva tracks. The physical parameters derived for the sources are basically unchanged. Symbols are as in Figure 6.
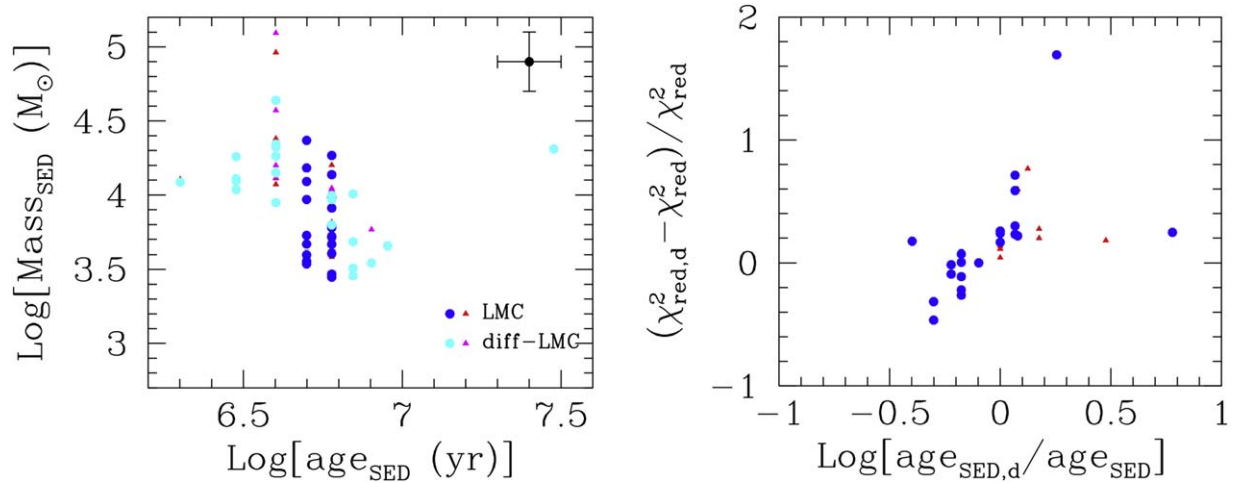
Figure 9. Left: the best-fit ages and masses for the 34 sample sources derived using the Geneva tracks with the LMC extinction curve (our default model; blue and red symbols are for high- and low-significance fits, respectively) and with the differential-LMC extinction for emission lines and stellar continuum (see Section 6; cyan and magenta symbols are for high- and low-significance fits, respectively). A representative error bar is shown, to aid clarity in the plot. Right: the fractional change in the goodness-of-fit as a function of the difference in age between the differential-LMC and standard LMC extinctions. The subscript "d" indicates values obtained with the differential-LMC extinction curve. Blue and red symbols are used as in previous Figures: blue circles for $\chi^2_{\rm red} \leqslant 6$ and red triangles for lower significance.

mass–age anticorrelation, typical of luminosity-limited observations subject to size-of-sample effects (Hunter et al. 2003). Separating the radio thermal sources in two groups, younger and older than 4 Myr, the younger group includes eight sources with median age 2.9 Myr and median mass $7 \times 10^3 \, M_\odot$, while the older group comprises five sources with median age 4.8 Myr and median mass $24 \times 10^3 \, M_\odot$. The older group is closer in age to our dust-buried sample, and is a factor of $\gtrsim 4$ more massive (Figure 6, left panel). That our sources are less massive, on average, than the Reines et al. (2008) sources when considering equal-age bins should not be surprising. This reflects, again, a combination of size-of-sample effect (Hunter et al. 2003) and sensitivity limits of the radio data. In addition, the selection function we apply to our sources may potentially remove the most massive clusters (see Section 8.2).

Several of the sources in our sample are located a few hundred parsecs away from the closest areas of bright Hα and Paβ emission; they are unlikely to have formed in these more (optically) active regions, since they would not have had the time to travel that far from their natal site. Assuming a (generous) speed of $10 \, {\rm km \, s^{-1}}$, the typical source would have traveled about 50–60 pc in 5–6 Myr, less than their distance from the more optically active regions. Furthermore, most sources are located at the periphery of areas where the optical light is depressed but the dust emission is strong, marking the location of dust clouds (Figure 10, right, and Figure 11). Our stellar clusters are, thus, likely to be in the process of emerging from these dust clouds. They may be the "tip of the iceberg" of larger numbers of clusters that are forming within the IR–bright dust clouds and are undetected because of the large dust column densities. These completely hidden sources will be primary targets for JWST studies.[12]

In summary, our sources are likely to be relatively young stellar clusters born in situ and still affected by significant dust attenuation, $A_V > 6$ mag. These clusters are young, but not extremely young, clustering around an age of 5–6 Myr.

---
[12] JWST Cycle 1 imaging for NGC 4449 is part of program No. 1783.

8.2. Where Are the Youngest Sources?

Our selection criteria place strong constraints on the type of sources we are likely to isolate. The constraint on the colors excess, $E(B - V) \gtrsim 2.1$ mag, has been already discussed in Section 4. As discussed earlier, selection effects on the EW(Paβ) limit our maximum age to be younger than 6–7 Myr. Below this age limit, we would expect roughly a constant number of clusters in each age bin, if star formation has continued at the same level over the past 6-10 Myr; yet only one cluster candidate, out of 34, has an age consistent with 2 Myr, with a poor fit to its SED (Table 4). Even adopting the results from the differential-LMC extinction fits for the cases where this choice yields lower values of $\chi^2_{\rm red}$ than the standard LMC extinction, we find six sources with ages between 3 and 4 Myr, and none with a best-fit age lower than 3 Myr.

There are several concomitant selection effects that are likely preventing us from securing the youngest, dust-buried sources. Sources younger than 3 Myr in the same mass and color excess range as the sources we select (Table 4) would be intrinsically brighter in line emission: a 2 Myr old stellar cluster has a luminosity in the hydrogen recombination lines that is about 10 times brighter than a 5 Myr old stellar cluster, at constant mass (Leitherer et al. 1999). Thus, a 2 Myr old, $10^{3.7} \, M_\odot$ cluster would be detectable in Hα, violating one of our selection criteria, which requires marginal or nondetection in the Hα line above the local diffuse emission. In order to remain within our selection criteria, the younger cluster would need to be about 10 times less massive than the older one. This implies that 2 Myr old clusters would need to have masses in the range 300–2500 $M_\odot$, with median mass $\sim 500 \, M_\odot$. Stellar clusters with these masses are subject to strong stochastic sampling, and highly likely to lack massive, ionizing stars (Fumagalli et al. 2011; Krumholz et al. 2015). A factor 10 decrease in mass, from $\sim 5000 \, M_\odot$ to $\sim 500 \, M_\odot$ corresponds to a factor ~ 3 increase in uncertainty in the ionizing photon flux, from $\sim 30\%$ to $\sim 100\%$ (Cerviño et al. 2002). However, a $500 \, M_\odot$, 2 Myr old cluster would also violate the constraints on the continuum photometry in the J and H bands, since a cluster's intrinsic luminosity does not change significantly in these bands between 2 and 5 Myr; thus, a $500 \, M_\odot$ cluster would be too

Table 5
Source Location and Photometry

ID (1)	R.A.(2000), Decl.(2000) (2)	F275W (3)	F336W (4)	F435W (5)	F555W (6)	F550M (7)	F658N (8)	F814W (9)	F110W (10)	F128N (11)	F160W (12)	L(Paβ) (13)	EW(Paβ) (14)
1	12:28:13.6083, +44:05:16.888	<32.326	<32.054	<32.090	<32.084	<32.169	32.664 ± 0.413	33.268 ± 0.104	33.736 ± 0.032	33.868 ± 0.076	33.706 ± 0.039	35.528 ± 0.078	1.806 ± 0.086
2	12:28:13.1596, +44:05:13.457	<32.115	<31.843	<31.879	<31.872	<31.958	32.713 ± 0.370	33.430 ± 0.086	33.570 ± 0.039	33.683 ± 0.095	33.443 ± 0.053	35.365 ± 0.097	1.838 ± 0.109
3	12:28:13.6158, +44:05:21.239	<32.012	<31.739	<31.776	<31.769	<31.854	32.449 ± 0.516	33.152 ± 0.119	33.872 ± 0.028	33.931 ± 0.071	33.845 ± 0.034	35.306 ± 0.073	1.445 ± 0.080
4	12:28:13.0039, +44:05:25.485	<31.966	<31.694	<31.730	<31.724	<31.809	32.449 ± 0.569	32.988 ± 0.143	33.359 ± 0.049	33.564 ± 0.108	33.472 ± 0.051	35.276 ± 0.111	1.881 ± 0.123
5	12:28:12.0411, +44:05:19.530	<32.228	<31.955	<31.991	<31.985	<32.070	32.914 ± 0.291	33.134 ± 0.121	33.824 ± 0.030	33.876 ± 0.076	33.696 ± 0.040	35.363 ± 0.078	1.581 ± 0.086
6	12:28:11.8231, +44:05:16.022	<32.472	<32.200	<32.236	<32.229	<32.313	32.989 ± 0.271	33.449 ± 0.085	33.783 ± 0.031	33.873 ± 0.076	33.755 ± 0.037	35.396 ± 0.078	1.625 ± 0.086
7	12:28:11.2588, +44:05:33.491	<32.852	<32.578	<32.616	<32.609	<32.694	33.061 ± 0.275	33.549 ± 0.076	33.721 ± 0.033	33.815 ± 0.081	33.689 ± 0.040	35.358 ± 0.083	1.650 ± 0.091
8	12:28:11.0066, +44:05:50.971	<32.933	<32.660	<32.696	<32.689	<32.775	33.393 ± 0.162	33.200 ± 0.117	33.557 ± 0.041	33.727 ± 0.090	33.495 ± 0.051	35.488 ± 0.093	1.956 ± 0.104
9	12:28:10.4670, +44:05:38.820	<32.393	<32.119	<32.157	<32.150	<32.235	32.464 ± 0.584	33.050 ± 0.134	33.577 ± 0.039	33.701 ± 0.093	33.575 ± 0.046	35.308 ± 0.095	1.734 ± 0.105
10	12:28:12.0334, +44:06:02.626	<32.366	<32.092	<32.129	<32.123	<32.208	32.848 ± 0.321	33.092 ± 0.127	33.753 ± 0.032	33.875 ± 0.076	33.737 ± 0.038	35.489 ± 0.078	1.744 ± 0.086
11	12:28:08.5375, +44:05:12.052	<32.630	<32.356	<32.394	<32.387	<32.472	33.433 ± 0.155	33.409 ± 0.089	33.940 ± 0.026	34.014 ± 0.065	33.832 ± 0.034	35.563 ± 0.066	1.660 ± 0.074
12	12:28:08.8027, +44:05:16.732	<32.687	<32.415	<32.451	<32.444	<32.529	32.638 ± 0.503	33.451 ± 0.085	33.948 ± 0.026	34.017 ± 0.065	33.834 ± 0.034	35.558 ± 0.066	1.648 ± 0.074
13	12:28:08.9467, +44:05:16.868	<32.439	<32.168	<32.203	<32.197	<32.282	32.449 ± 0.880	32.768 ± 0.186	33.267 ± 0.055	33.576 ± 0.107	33.623 ± 0.043	35.261 ± 0.110	1.843 ± 0.123
14	12:28:09.5793, +44:05:11.430	<33.203	<32.932	<32.967	<32.962	<33.047	33.201 ± 0.962	33.435 ± 0.093	34.032 ± 0.025	34.129 ± 0.057	33.988 ± 0.029	35.694 ± 0.059	1.680 ± 0.065
15	12:28:10.2393, +44:05:12.852	<33.171	<32.897	<32.935	<32.928	<33.013	34.008 ± 0.164	34.327 ± 0.032	34.507 ± 0.015	34.532 ± 0.036	34.365 ± 0.019	35.902 ± 0.037	1.439 ± 0.041
16	12:28:10.6461, +44:05:18.892	<32.583	<32.310	<32.347	<32.340	<32.424	32.449 ± 0.753	32.924 ± 0.156	33.852 ± 0.029	33.999 ± 0.066	33.938 ± 0.030	35.580 ± 0.068	1.700 ± 0.075
17	12:28:09.2287, +44:05:28.172	<32.472	<32.200	<32.236	<32.229	<32.314	32.449 ± 0.576	32.707 ± 0.200	33.665 ± 0.035	33.742 ± 0.088	33.479 ± 0.051	35.370 ± 0.091	1.764 ± 0.101
18	12:28:12.3614, +44:05:38.604	<32.820	<32.548	<32.584	<32.576	<32.661	32.449 ± 0.678	33.493 ± 0.081	33.660 ± 0.036	33.804 ± 0.082	33.605 ± 0.045	35.508 ± 0.085	1.871 ± 0.094
19	12:28:13.5209, +44:06:15.261	<32.853	<32.579	<32.617	<32.610	<32.695	33.262 ± 0.197	33.630 ± 0.070	33.608 ± 0.038	33.748 ± 0.088	33.489 ± 0.051	35.483 ± 0.090	1.917 ± 0.102
20	12:28:12.7311, +44:06:14.889	<32.531	<32.257	<32.295	<32.287	<32.373	32.714 ± 0.418	33.153 ± 0.119	33.535 ± 0.041	33.690 ± 0.094	33.517 ± 0.049	35.395 ± 0.096	1.870 ± 0.107
21	12:28:14.6910, +44:06:29.325	<32.072	<31.799	<31.836	<31.829	<31.914	32.697 ± 0.374	33.431 ± 0.086	33.549 ± 0.040	33.651 ± 0.098	33.530 ± 0.048	35.206 ± 0.100	1.665 ± 0.110
22	12:28:14.9099, +44:06:21.084	<32.417	<32.145	<32.181	<32.174	<32.259	32.591 ± 0.452	32.813 ± 0.176	33.508 ± 0.042	33.652 ± 0.098	33.424 ± 0.054	35.374 ± 0.101	1.897 ± 0.112
23	12:28:14.3714, +44:06:44.803	<32.181	<31.908	<31.945	<31.938	<32.022	32.967 ± 0.265	33.807 ± 0.056	33.559 ± 0.039	33.723 ± 0.090	33.494 ± 0.050	35.474 ± 0.093	1.942 ± 0.103
24		<32.096	<31.824	<31.860	<31.854	<31.939	32.449 ± 0.552	33.091 ± 0.127	33.270 ± 0.054	33.426 ± 0.127	33.181 ± 0.072	35.180 ± 0.130	1.944 ± 0.146

Table 5
(Continued)

ID (1)	R.A.(2000), Decl.(2000) (2)	F275W (3)	F336W (4)	F435W (5)	F555W (6)	F550M (7)	F658N (8)	F814W (9)	F110W (10)	F128N (11)	F160W (12)	L(Paβ) (13)	EW(Paβ) (14)
	12:28:13.2234, +44:06:47.993												
25	12:28:13.9051, +44:06:03.009	<32.537	<32.266	<32.301	<32.295	<32.380	32.449 ± 0.579	32.553 ± 0.243	33.922 ± 0.027	33.965 ± 0.069	33.803 ± 0.035	35.403 ± 0.070	1.520 ± 0.078
26	12:28:11.7727, +44:06:00.424	<32.532	<32.258	<32.295	<32.289	<32.374	32.449 ± 0.710	33.160 ± 0.118	33.466 ± 0.044	33.624 ± 0.101	33.382 ± 0.057	35.372 ± 0.104	1.936 ± 0.116
27	12:28:10.6799, +44:06:01.920	<32.188	<31.916	<31.952	<31.945	<32.030	32.729 ± 0.368	33.112 ± 0.124	33.619 ± 0.037	33.653 ± 0.098	33.533 ± 0.048	34.979 ± 0.100	1.390 ± 0.109
28	12:28:10.6474, +44:06:01.332	<32.129	<31.856	<31.892	<31.886	<31.971	32.449 ± 0.603	32.318 ± 0.311	33.144 ± 0.063	33.380 ± 0.134	33.123 ± 0.077	35.224 ± 0.138	2.095 ± 0.156
29	12:28:10.1293, +44:06:12.579	<32.093	<31.821	<31.858	<31.851	<31.936	32.725 ± 0.359	32.608 ± 0.222	33.600 ± 0.038	33.698 ± 0.093	33.615 ± 0.044	35.193 ± 0.095	1.590 ± 0.104
30	12:28:11.4805, +44:04:59.731	<32.173	<31.901	<31.937	<31.930	<32.015	33.053 ± 0.243	32.800 ± 0.178	33.646 ± 0.036	33.829 ± 0.080	33.867 ± 0.033	35.339 ± 0.082	1.608 ± 0.090
31	12:28:14.4625, +44:05:05.845	<32.365	<32.092	<32.129	<32.122	<32.207	33.134 ± 0.220	33.025 ± 0.137	33.633 ± 0.036	33.789 ± 0.084	33.608 ± 0.044	35.497 ± 0.086	1.876 ± 0.096
32	12:28:14.8929, +44:05:35.564	<32.295	<32.022	<32.059	<32.051	<32.137	32.449 ± 0.530	32.820 ± 0.174	33.335 ± 0.051	33.535 ± 0.112	33.268 ± 0.065	35.347 ± 0.116	2.042 ± 0.130
33	12:28:14.7671, +44:05:46.484	<32.590	<32.318	<32.354	<32.348	<32.433	32.739 ± 0.378	33.144 ± 0.121	33.415 ± 0.047	33.553 ± 0.110	33.360 ± 0.059	35.243 ± 0.113	1.851 ± 0.126
34	12:28:15.0205, +44:05:49.044	<31.987	<31.714	<31.751	<31.744	<31.829	32.539 ± 0.464	33.044 ± 0.134	33.234 ± 0.057	33.380 ± 0.134	33.195 ± 0.071	35.077 ± 0.137	1.862 ± 0.153

Notes.

(1) The identification number of the source.

(2) R.A. and decl. in J2000 coordinates.

(3)–(12) Logarithm of the luminosity density of each source in the indicated filter, in units or erg s^{-1} Å^{-1}. The photometry is measured in circular apertures with 3 px (0″12) radius on the plane of the sky. Aperture corrections and corrections for the attenuation due to the foreground dust from the Milky Way have been applied to the listed photometry. See the text for more details.

(13) The logarithm of the luminosity in the Paβ emission line, in units of erg s^{-1}.

(14) The logarithm of the EW of Paβ, in Å, calculated from the ratio of the emission-line flux to the stellar continuum flux density.
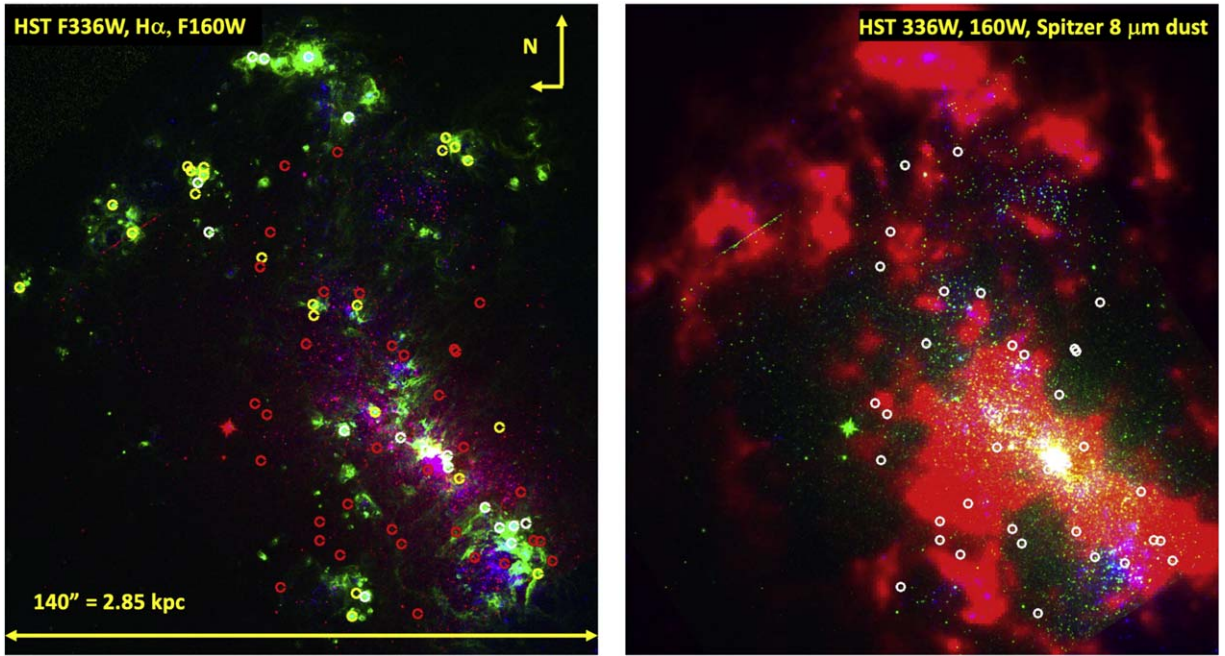
(This table is available in machine-readable form.)

Figure 10. Left: a three-color composite of NGC 4449 using F336W (blue), continuum-subtracted Hα+[N II] (green), and F160W (red). The FOV is 2′.5 × 2′.5 (3.05 × 3.05 kpc²), slightly larger than the FOV of WFC3/IR to show the location of all of the Reines et al. (2008) sources. The 39 Reines et al. (2008) sources were identified from multiwavelength Very Large Array (VLA) data (see the text) and include thermal/likely thermal/mixed sources (white circles) and nonthermal/uncertain sources (yellow circles). Our sources, identified from the stellar-continuum-subtracted Paβ WFC3/IR image, are shown as red circles. All circles have a radius of 1″0 to facilitate visualization. North is up, East is left. Right: a three-color composite of HST (F336W = blue and F160W = green) and Spitzer 8 μm dust (red) images, showing the location of our sources (white circles) relative to the location of the dust emission. This figure shows a larger dynamical range for the 8 μm dust emission than Figure 1, to highlight that our sources are generally located at the margins of emission peaks.
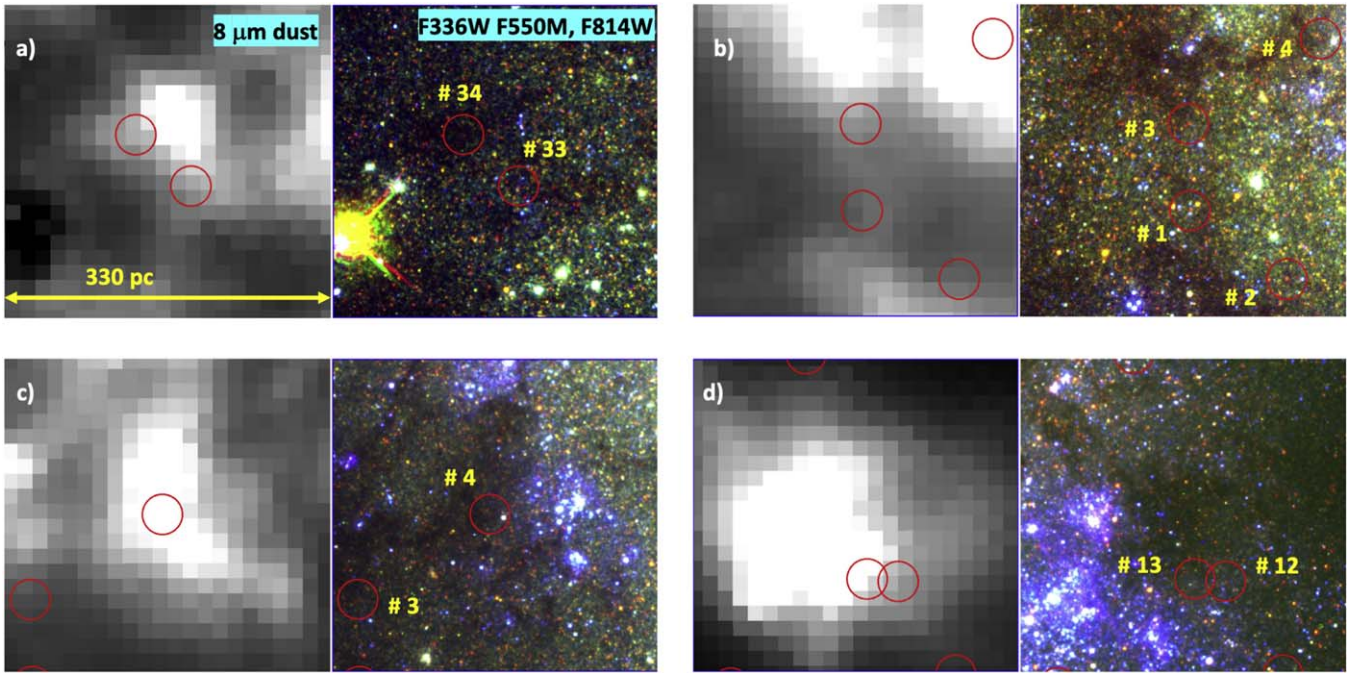

Figure 11. The location of several of our sources is shown in four separate panels (a), (b), (c), and (d) displaying cutouts of the 8 μm dust map (left of each panel, in b/w) and of a three-color composite using F336W (blue), F550M (green), and F160W (red, right of each panel). All cutouts have a size of 330 pc. The three HST continuum bands are chosen to explicitly avoid any line emission, to highlight the location of dust lanes and clouds. Our sources are shown as red circles, marked with the ID number from Table 5. Source #4 is shown twice, both in panels (b) and (c), to better highlight the dusty region it is sitting on. All circles have a radius of 1″0 to facilitate visualization. North is up, east is left.

faint to fit the observed J and H fluxes. In other words, clusters younger than the ages we derive, ∼5–6 Myr, still need to have masses with a median ∼5000 $M_\odot$ to fit the broadband photometry.

Alternatively, a 2 Myr old, $10^{3.7}$ $M_\odot$ stellar cluster could become undetectable in Hα if it is subject to a larger amount of dust extinction than we derive from SED fitting. Depressing the Hα luminosity by an additional order of magnitude requires
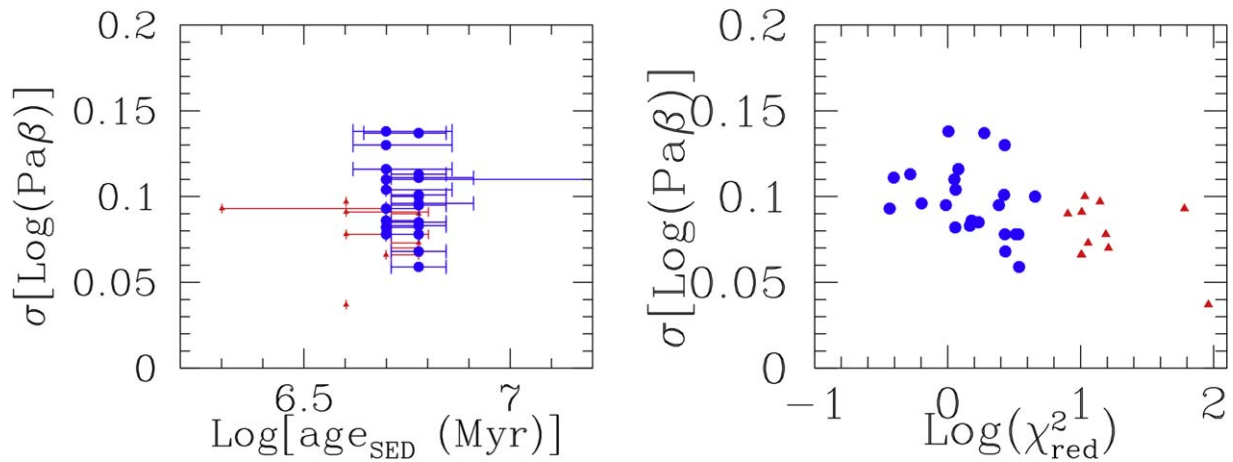
Figure 12. The measurement uncertainty in the Paβ luminosity as a function of the best-fit age, age$_{SED}$ (with its 1σ uncertainty, left), and of the χ^2_{red} value of the fits (right), both from Table 4.

A_V to increase from a median value of 8.6 mag to a median value of ~ 11.7 mag. In this case, the observed flux in the I, J, and H bands would decrease by factors of 5.4, 2.5, and 1.8, respectively, lowering the median I-band luminosities to values that have $S/N \lesssim 1$. This is too low of a limit for our visual classification to recognize the sources as real detections in that band; hence, those sources would not have entered our sample. Young clusters more massive than $10^{3.7}\,M_\odot$ would proportionally require higher A_V values to become undetectable in $H\alpha$, making them also too faint in the I band. In summary, the combination of our detection limits and selection criteria causes sources younger than 3–4 Myr to be excluded from our sample. Thus, we are not excluding their existence in the galaxy, just their presence in our sample.

An additional selection effect comes from our detection requirements for *both* $H\alpha$ and Paβ, meaning that while we want $H\alpha$ to remain undetected, we still require Paβ to be detected with $S/N \geqslant 3$ and to be sufficiently isolated from neighboring regions as to provide a reliable photometric measurement. This requirement excludes the most crowded (in nebular emission) regions in the galaxy, which are also the brightest and where we would expect the youngest and most-massive clusters to be located. Therefore, dust-buried regions younger than 3–4 Myr may be located in areas excluded from our search, further reinforcing the conclusion above that they are likely to be present in the galaxy, but not included in our sample. The comparison with the radio sources detected by Reines et al. (2008), discussed in the previous subsection, lends support to this scenario. Given all of this, it is perhaps not surprising that we do not isolate very young, dust-buried stellar clusters.

8.3. Could These Be Spurious Sources or Spurious Ages?

Because these are unusual sources, the potential that they might be spurious sources needs to be considered. As discussed in Section 4, our sources are unlikely to result from artifacts in the stellar continuum subtraction of the near-IR narrowband filter (F128N). Visual inspection of the continuum-subtracted F658N image enables us to exclude oversubtraction in this image that would generate artificial "nondetections" in $H\alpha$.

We also exclude the possibility that these could be background galaxies. The I-band magnitude range of our sources is $I_{AB} = 20.6$–25.6 mag; thus, the faint end overlaps with the bright end of the V-band dropouts at redshift $z \sim 5$

(Stark et al. 2009). However, our Paβ line emission would correspond to a line emission at rest-frame wavelength $\lambda_{rest} \sim 0.21\,\mu m$ in a $z \sim 5$ galaxy. No known emission line exists at this wavelength, which allows us to exclude high-redshift interlopers.

The SED fits could be biased, if, for instance, the uncertainties in the F128N filter, which is also the shallowest among the near-IR ones, were to drive the ages from the fits or the goodness-of-fit. We test this by plotting the uncertainties on the Paβ luminosities as a function of both the ages and the χ^2_{red} values (Figure 12). We see from the plots that while there is no correlation between ages and uncertainties in Paβ, $\sigma[Log(Pa\beta)]$, there is a weak trend between χ^2_{red} and $\sigma[Log(Pa\beta)]$, in the sense that larger uncertainties yield better fits. However, this trend is extremely weak and only driven by a small number of data: the 1σ vertical scatter on the high-significance data ($\gtrsim 0.04$ two-sided) is comparable with the dynamical range of the data (~ 0.08); the majority of the data do not present a significant correlation between the two quantities, implying that smaller uncertainties do not correspond necessarily to worse SED fits.

Although we have excluded the impact of stochastic sampling of the stellar IMF in our analysis, we reconsider this possibility here. The reason is because our SED-fit ages are mainly constrained by the presence of Paβ emission, i.e., by the presence of massive, ionizing stars (>10–$15\,M_\odot$). If, for any reason, our assumption that the IMF is fully sampled is not correct, the ages would be different from those we derive. We consider the case that the sources we select happen to be all sources that have failed to produce the most massive stars; in other words, we still need at least a few stars with mass $>15\,M_\odot$ to be present in order to generate the hydrogen line emission, but above this mass, the IMF is not fully sampled. In this scenario, the hydrogen recombination lines would be intrinsically less bright than those of a fully sampled IMF all the way to $120\,M_\odot$. The consequence is that our dust-buried sources could be younger, or span a broader range of ages, than what we derive from the SED fits. The counterargument is that the spatial distribution of the dust-buried sources is different from that of the low-dust sources discussed in the next subsection, although they span a similar range in both age and mass. Thus, we would need to invoke a physical mechanism that, at the same time, segregates stellar clusters spatially within

the galaxy and in massive star content. In the absence of an obvious mechanism for this, we discard this possibility, at least for the moment.

We now discuss our model assumption of a 0.5 gas covering factor, i.e., 50% of ionizing photons absorbed by the gas surrounding the cluster. For our dust-buried sources, we may expect a higher gas covering factor, since an H II region placed within a dense environment can be expected to be compact. If we choose a 1.0 covering factor (YGGDRASIL only offers 0, 0.5, and 1.0 covering factors), we find that the best-fit ages increase slightly, from a median value of $\sim$5.5 Myr to a median value of $\sim$6 Myr; in addition, all high-significance ($\chi^2_{\rm red} \leqslant 6$) sources now are 6 Myr old. This is easily understood by remembering that our ages are mainly determined by the EW(Paβ); higher gas covering factors translate into brighter emission lines and larger EWs in the models, implying that older ages are required to match the observations. The average color excess decreases only slightly, by about 0.05 mag, which is understood by recalling that in our fits the color excess value is mainly determined by the shape of the stellar continuum. The derived stellar masses also decrease a little on average, by $\sim$0.15 dex, but nonuniformly across the clusters; the new masses are still in the range 3000–25,000 $M_\odot$. Finally, there is no change in the number of high/low-significance fits: the high-significance fits with the 0.5 covering factor models remain high-significance with the 1.0 covering factor models. Thus, covering factors in the range 0.5–1.0 yield almost identical results for the best-fit parameters of our dust-buried stellar clusters.

We test the impact of our choices of population models and fitting approach by running the stellar population inference code Prospector (Johnson et al. 2021) on the photometry of our sources. While Prospector may not be the best choice for SSPs at the extremely young ages of our sources, it represents, nevertheless, a completely different approach, both in terms of fitting and of stellar population libraries (Conroy et al. 2009; Conroy & Gunn 2010; Falcón-Barroso et al. 2011; Choi et al. 2016; Dotter 2016; Speagle 2020). We use flat priors in mass, extinction, and age, spanning the full physical range for clusters, but fix the metallicity at 40% solar, as appropriate for NGC 4449. The output physical parameters track well our main results, with the main discrepancies between the two approaches found for our low-significance clusters. For our high-significance clusters, Prospector yields less-massive solutions (about half the mass we derive with our approach), with similar ages (median age = 6 Myr) but a broader range 5–15 Myr and larger uncertainties (ΔLog(Age) $\sim$ 0.8), and similar attenuation values. Only two of the high-significance clusters (# 7 and # 18) are found by Prospector to be older, $\sim$15 Myr, and less attenuated, $E(B - V) \sim$1.3–1.4 mag, than what we find with our default approach. We conclude that a different fitting approach from our adopted one does not yield a sample of very young sources; the clusters are still relatively old and with significant foreground extinction.

One remaining source of bias in our age determinations is absorption of LyC photons by dust (Dopita et al. 2003). In this case, the ionizing photons produced by the massive stars are directly absorbed by dust before they can ionize the gas, thus decreasing the number of free electrons and recombination cascades and, as a consequence, depressing the luminosity of nebular lines and continuum. We use the results from the models of Krumholz & Matzner (2009), Draine (2011), and

Yeh et al. (2013) to guide this part of the analysis. According to these models, for dust to significantly absorb ionizing photons, the hydrogen inside the H II region needs to be highly ionized, because neutral hydrogen has a much larger cross section than dust for ionizing photon absorption. The high ionization increases the radiation pressure, which thus "pushes" the ionized gas into a shell creating a cavity within the H II region. In this configuration, most of the ionizing photon absorption now occurs in the shell, which is also where the neutral gas lives, in turn limiting the effectiveness of the dust absorption. The result is a "floor" of about 50%–70% to the maximum number of ionizing photons that can be directly absorbed by dust at solar metallicity, and this number decreases for decreasing metal abundances (Draine 2011). A $\sim$4 Myr old stellar cluster has an EW(Paβ) that is $\sim$17 times larger than that of a 6 Myr old stellar cluster (from Starburst99; Leitherer et al. 1999). Thus, in order for a 4 Myr old cluster to "mimic" a 6 Myr old cluster through our SED fitting approach, dust would need to directly absorb $\sim$94% of the ionizing photons and suppress the Paβ line emission accordingly. This is a much larger fraction than the "floor" discussed above, which enables us to disfavor direct absorption of LyC photons by dust as a driver for the best-fit ages.

8.4. Comparison with the Young, Low-dust Cluster Population

The LEGUS project (Calzetti et al. 2015b) isolated stellar cluster candidates in this galaxy, as well as other galaxies, which were then visually inspected by LEGUS team members and classified according to four categories: 1, 2, 3 for stellar clusters or compact associations, and 4 for everything else (contaminant, interlopers, stars with diffuse halos, etc.). Details on the selection and visual classification of the stellar cluster candidates are given in Adamo et al. (2017). We summarize here the characteristics of the selection and identification that are relevant to this work. The LEGUS observations covered the five bands NUV, U, B, V, and I (WFC3/F275W, F336W, F438W, F555W, and F814W; where possible, archival ACS/F435W, F555W, and F814W images were used), and cluster candidates were selected from a white-light image obtained from combining the images in all five bands (Calzetti et al. 2015b). The automatically selected stellar clusters were then visually inspected when brighter than $M_{V,\rm Vega} = -6$ mag, which corresponds to a mass of a few hundred $M_\odot$. The magnitude cut was imposed after aperture correction, using an average value for the latter (Adamo et al. 2017). Whitmore et al. (2020) added the Hα filter to expand the parameter space for selecting stellar clusters and expanded the existing catalog with visually selected clusters slightly fainter than the -6 mag limit; these authors produced a final catalog of 594 stellar clusters in the $1 + 2 + 3$ classes. The catalog expansion of Whitmore et al. (2020) has no impact on our analysis since we limit our comparisons to young clusters more massive than $\sim$3000 $M_\odot$, which are also brighter than $M_{V,\rm Vega} = -6$ mag.

As detailed in Adamo et al. (2017), the SEDs of all cluster candidates detected in at least four of the five bands were fit with the same SSP models used in this work, using a similar treatment of the dust attenuation. The requirement that the clusters have to be detected in four out of five bands means that either the NUV (F275W) or the U (F336W) are included in the fits, which imposes a maximum limit on the amount of attenuation in each cluster since the clusters need to be detected at blue wavelengths. The analysis performed by Whitmore et al. (2020) on the
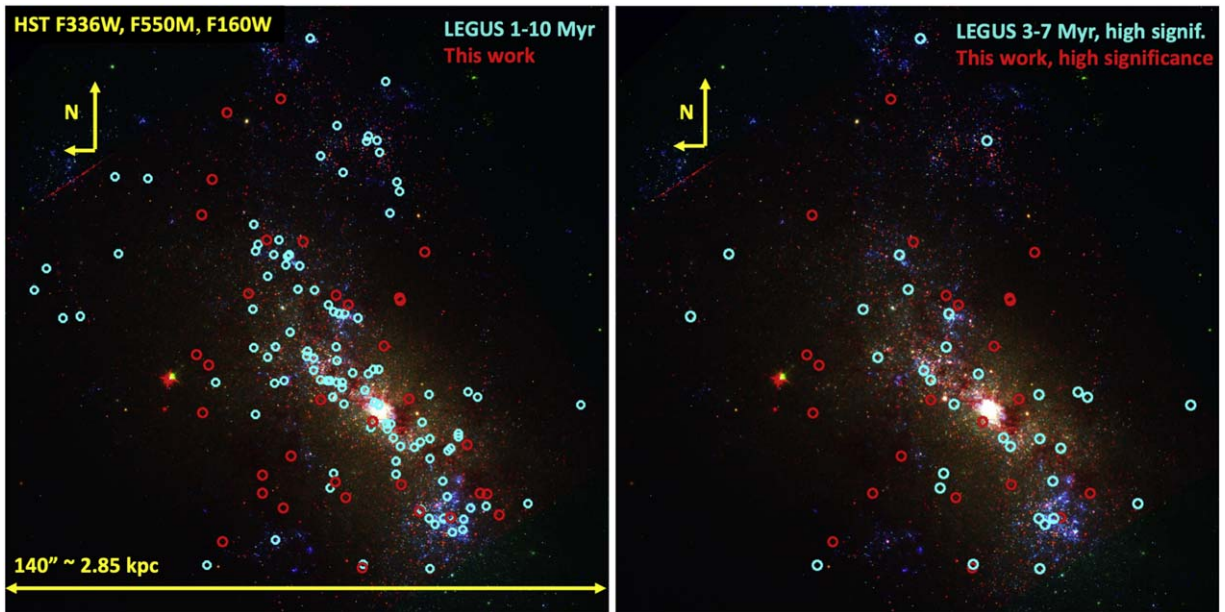
Figure 13. Left: the location of the LEGUS stellar clusters with age 1–10 Myr and mass $\geqslant 3000\,M_\odot$ (cyan circles) and of our dust-buried sources (red circles) is shown on a three-color composite using F336W (blue), F550M (green), and F160W (red). Only the LEGUS sources located within the WFC3/IR footprint are shown here. Right: the same as the left panel, but restricting both types of sources to the high-significance ones: $\chi^2_{\rm red} \leqslant 10$ for the LEGUS sources (cyan circles; Adamo et al. 2017) and $\chi^2_{\rm red} \leqslant 6$ for the dust-buried sources (red circles). The LEGUS sources are further restricted to the age range 3–7 Myr to better match the age range of the dust-buried sources.

LEGUS stellar cluster population confirms the maximum observed $E(B-V) \lesssim 1$ mag.

The physical parameters, age, mass and $E(B-V)$, provided in the LEGUS catalogs are from the Yggdrasil SSPs attenuated by the Milky Way extinction (Fitzpatrick et al. 2019) and the starburst attenuation curves, only. Of the different "flavors" of catalogs available, we use those with aperture corrections derived from isolated clusters measured in the images (Adamo et al. 2017), which matches our approach to aperture photometry correction. We update the LEGUS masses to account for the slight difference in adopted distance for NGC 4449 (3.9 Mpc for LEGUS versus 4.2 Mpc here). We select all clusters (classes 1, 2, and 3) with age $\leqslant 10$ Myr and mass $\geqslant 3000\,M_\odot$, detected in at least four filters. The are 56 such sources from the Milky Way extinction catalog and 127 from the starburst attenuation catalog, 43 and 106 of which, respectively, are within the footprint of the WFC3/IR images. The difference in source numbers between the two cases is easily understood in terms of the difference in shape between the two curves in the NUV (e.g., Calzetti et al. 1994). The Milky Way extinction curve has a strong feature at 0.2175 μm while the starburst curve has none, and the wings of this feature enter in the F275W filter. Thus, if the dust attenuation in NGC 4449 does not have intrinsically strong absorption at 0.2175 μm, the application of the Milky Way extinction to red SEDs will inevitably yield old ages and low extinctions to "force" the fit of the F275W filter. Conversely, the application of the starburst curve enables a wider range of ages and attenuations. We retain only the catalog that uses the starburst attenuation curve to derive the physical parameters, as this case is likely to be more representative of exposed or partially exposed clusters. The distribution of the LEGUS sources relative to the dust-buried sources from this work is shown in Figure 13, left.

Figure 14 shows the mass versus age and the $E(B-V)$ versus age plots of our sources (blue and red symbols as

before) overlaid on top of the same parameters for the 106 LEGUS sources (cyan and magenta symbols). The cyan symbols identify the 53 sources with $\chi^2_{\rm red} \leqslant 10$, thus those that have high-fidelity SED fits (Adamo et al. 2010). Of these, 32 (16) have ages between 3 (4) and 7 Myr, to be compared with our 23 high-fidelity sources (Figure 13, right). The two samples overlap in mass range, although the LEGUS sample extends to higher mass values, almost $10^6\,M_\odot$, than our sample. This is due to the selection function for our sources, which imposes low significance or nondetections in Hα, thus excluding high-mass (brighter) sources. However, the two samples occupy different spatial locations within the galaxy, with the LEGUS high-fidelity, 3–7 Myr sources located mainly along the bright ridge of star formation and the dust-buried sources distributed more homogeneously throughout the FOV (Figure 13, right). All selected LEGUS sources have $E(B-V) \lesssim 1$ mag, as already discussed. Thus, our sources and the LEGUS sources occupy two distinct loci in the $E(B-V)$ parameter space, as can be expected since the two samples have been selected with drastically different properties: UV and optically faint for our sources and UV detected for the LEGUS sources. Further comparisons would need to take into account the differences between the two samples, including differences in the SED fitting approach and wavelength range; however, we note that, within a similar age range, they contain comparable numbers of sources. This indicates that our sample is not simply a collection of rare outliers, but represents a population of dust-buried clusters with a comparable census as the low-dust clusters.

8.5. The Location of the Dust-buried Clusters

Given the dusty nature of our sources and their location in correspondence of dust lanes/clouds, we consider the possibility that our selection criteria isolate stellar clusters that have emerged on *the far side* of the galaxy or of the clouds where
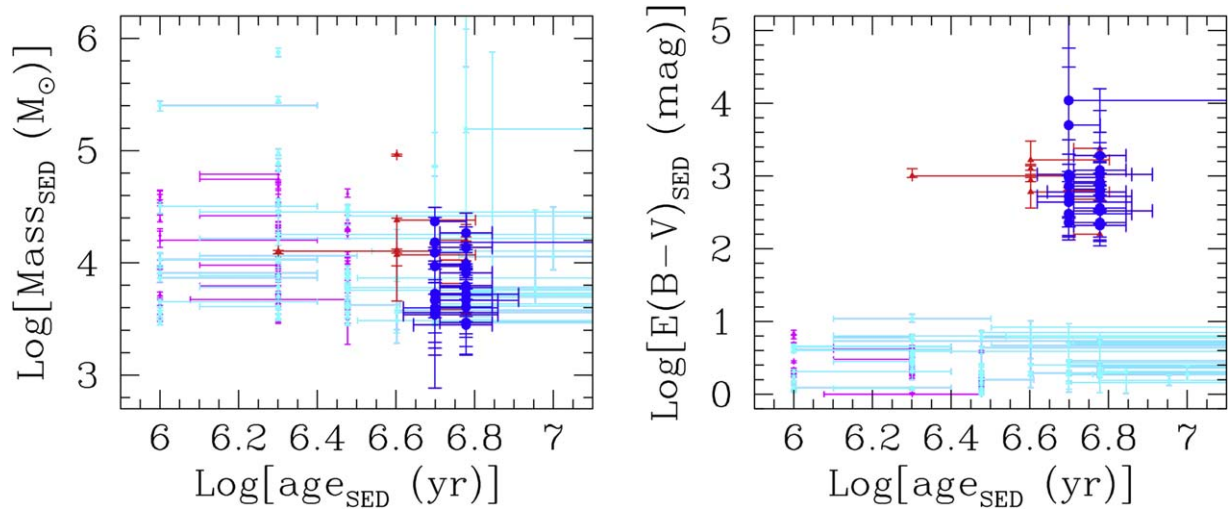
Figure 14. The stellar mass (left) and the color excess (right) as a function of the age derived from the SED fits, with 1σ uncertainties, for our sources (blue and red symbols) and for the LEGUS sources (cyan and magenta symbols). As in previous figures, blue symbols indicate sources with $\chi^2_{\rm red} \leqslant 6$ from the SED fits, while red symbols are for sources with larger values of $\chi^2_{\rm red}$. For the LEGUS sources, the cyan symbols are for sources with $\chi^2_{\rm red} \leqslant 10$ and magenta symbols for sources with larger values of $\chi^2_{\rm red}$.

they formed. We present two arguments to exclude this possibility: one based on the spatial distribution of the dust-buried and low-dust clusters and one based on the characteristics of the two populations.

We first evaluate whether the dust-buried clusters are located behind the galaxy's mid-plane dust. Measurements of the typical column densities of mid-plane diffuse dust indicate values of $A_V \lesssim 1$–1.5 mag in SDSS spiral galaxies (Holwerda et al. 2007). Even accounting for the inclination of NGC 4449 (Table 1), we obtain a line-of-sight column density of $A_V \sim 2.7$–4.0 mag for the mid-plane dust, which is significantly lower than the dust column densities we derive ($A_V > 6$ mag). In addition, several of our sources are located in the outskirts of the brightest areas of dust emission (Figure 11), suggesting that they are at the margins of actively star-forming, and possibly dense, regions. Both pieces of evidence suggest that the clusters in our sample are affected by local dust absorption, as can be caused by the colocation with natal clouds.

We use the census of dust-buried clusters to evaluate the possibility that these are clusters that have emerged on the *far side* of molecular clouds. Statistical considerations expect comparable numbers of stellar clusters to emerge from both the far side and the near side of clouds. Observationally, we expect to observe a larger number of clusters emerging from the near side of the cloud than the far side, for two reasons: (1) some of the *far side* clusters will be dimmed below detectability by the foreground dust; (2) existing models predict that natal molecular clouds get destroyed by stellar feedback, thus freeing stellar clusters of their dust. The "dark clouds," i.e., regions that are well detected both in the H-band filter and in the 8 μm dust map but are weakly emitting in the V band, occupy about 20% of the total star-forming area within the WFC3/IR FOV. Based on areal coverage arguments alone, we expect about five times more low-dust sources than dust-buried ones in the 3–7 Myr age range. We detect only 33% more high-significance low-dust clusters than dust-buried ones. The addition of undetectable, deeply dust-buried clusters is unlikely to change statistics significantly: the area of the dark clouds that have $A_V > 10$ mag, has low

filling factor (<0.1; Lada et al. 2009). For this estimate, we assume that young, low-dust clusters that are far away from any identified dark cloud were born in clouds that have since been destroyed. In a second estimate, we limit our calculation to the dark clouds hosting or in proximity of our 23 high-significance dust-buried clusters. In this case, we expect about equal numbers of dust-buried and low-dust clusters, and possibly larger numbers of low-dust clusters if some dust-buried ones are lost from census because they are so dimmed by dust to be undetectable. We count 13 low-dust clusters in the 3–7 Myr age range, i.e., about (or less than) one-half of what would be expected based on migration considerations alone.

The spatial arguments above, however, do not leverage the main characteristic of the dust-buried clusters: they show compact emission in the Paβ line, with EWs in the range 25–125 Å (Table 5). We measure the Paβ emission in the 53 low-dust, 1–10 Myr old clusters of the LEGUS sample, adopting the same photometric aperture of 0″12 radius used for our dust-buried sources. Prior to performing aperture photometry, we carefully determine the centroids of the low-dust clusters using the higher-resolution optical images. We find that only four low-dust clusters have detectable line emission within those apertures, with EW(Paβ) $\simeq 210$ Å, 165 Å, 4 Å, and 2 Å. All four clusters are younger than 3 Myr. The remaining 49 low-dust clusters are consistent with having zero Paβ line emission in the small photometric aperture, including all clusters with age $\geqslant 3$ Myr. Thus, none of the low-dust clusters have values of the EW(Paβ) matching those of our dust-buried population. A visual inspection of the continuum-subtracted Paβ and Hα images confirms that only four sources (8% of the total) have centrally peaked nebular emission. Of the remaining 49, 12 are located in areas with no nebular emission within a radius of ~ 40 pc, while the other 37 are surrounded by nebular emission shells, broken or whole, and filaments. Increasing the aperture to 0″20 (5 px) radius only adds two clusters with positive Paβ line detection, one younger than 3 Myr with EW(Paβ) $\simeq 1$ Å and one 5 Myr old with EW(Paβ) $\simeq 5$ Å.

As argued above, if the dust-buried clusters were truly low-dust clusters that have emerged on the far side of their natal

clouds, we would expect roughly equal numbers of clusters with similar properties that have emerged on the near side of the clouds. Alas, we find no low-dust clusters with compact Paβ line emission in the age range 3–7 Myr and none with EW(Paβ) in the range 25–125 Å irrespective of age; conversely, we have 23 dust-buried clusters with such characteristics. Under the assumption of a Poisson distribution for the spatial distribution of clusters, the probability of finding zero clusters on one side and 23 on the other side of clouds is $p(0)\sim 1 \times 10^{-10}$; even under the generous assumption that all four clusters younger than 3 Myr and with detected Paβ emission could resemble our dust-buried population, the probability $p(\leqslant 4) \sim 1.4 \times 10^{-6}$. The implication is that the low-dust and the dust-buried clusters represent two morphologically distinct populations. The low-dust, young stellar clusters are consistent with early gas clearing (e.g., Krumholz et al. 2019; Dinnbier & Walch 2020), while the dust-buried clusters appear to have retained their gas, as would occur if the gas were prevented from leaving the area of the clusters (see Section 8.6). The two populations could actually represent the two extremes of a continuum of properties, ranging from clusters that undergo early gas clearing to clusters that are resistant to gas clearing, possibly due to variations in local conditions.

Our estimates, therefore, indicate that a large fraction of the dust-buried clusters are truly embedded or partially embedded in their natal clouds and are unlikely to be sources that have emerged on the far side of the galaxy or the clouds.

8.6. Implications for the Emergence Timescale(s) of Stellar Clusters

Pre-SN feedback processes that are likely to be important for young stellar clusters in our mass and size range (3000–25,000 $M_{\odot}$, $\approx$1–3 pc, $v_{\rm esc} \sim 7\,{\rm km\,s}^{-1}$) include photoionization, direct radiation pressure, and stellar winds (Pellegrini et al. 2011; Dale et al. 2012; Krause et al. 2013; Krumholz et al. 2019), all of which have timescales of a few megayears, and should help clear the surrounding medium before the first SN explosion occurs at around $\sim$4 Myr (Leitherer et al. 2014). The presence of a population of young ($\sim$1–6 Myr) stellar clusters with low extinction values, as identified by the LEGUS collaboration (Whitmore et al. 2020), aligns with this framework of early gas dispersal from around the clusters.

Conversely, the population of dust-buried stellar clusters identified in this work does not support that general picture, and requires a different explanation. These clusters are old enough, according to their SED-derived ages of $\sim$5–6 Myr, that they should have experienced both pre-SN and SN feedback. We note that our results for the ages are robust against choices of the attenuation/extinction prescription. SNe may have not occurred yet if, due to incomplete sampling of the IMF, the clusters' most massive stars are $\lesssim 30\,M_{\odot}$ (i.e., lifetimes $\gtrsim 6$ Myr; Castelli & Kurucz 2003). Chevance et al. (2022) derived a range of SN timescales, $\sim$4–8 Myr for our cluster mass range, by including stochastic IMF sampling. These clusters, however, still contain sufficiently massive stars that they should have experienced pre-SN feedback (Leitherer et al. 2014) and performed some clearing of the surrounding medium; alas, they appear not to have done so. Using the measured $A_V \sim$ 6.5–11 mag range to estimate the gas column density in front of the clusters, we obtain $N({\rm H}) \sim (3.4–5.7) \times 10^{22}\,{\rm cm}^{-2}$ (Bohlin et al. 1978; Zhu et al. 2017), after including

that NGC 4449 has 40% solar metallicity and thus larger gas densities at given A_V than a solar metallicity source (Rémy-Ruyer et al. 2014). If the column of gas and dust in front of the dust-buried clusters is $\sim$20 pc in depth (i.e., half the radius of a typical molecular cloud in the Milky Way), the resulting density is: $n({\rm H}) = 550–920\,{\rm cm}^{-3}$. If the same density fully surrounds the stellar cluster, it is likely that the ejection and expansion of its gas in response to feedback has been stalled, as we discuss in the next paragraphs (e.g., Smith et al. 2006; Silich et al. 2007; Westmoquette et al. 2014; Zamora-Avilés et al. 2019).

The measured gas column densities correspond to an external pressure of $P_{\rm ext}/k_B = 3.9319 \times 10^{-39} N({\rm H})^2 = 0.5–1.3 \times 10^7\,{\rm K\,cm}^{-3}$, where $N({\rm H})$ is in units of ${\rm cm}^{-2}$ (the numerical constant is not adimensional); we neglect the contribution of the stellar component to the pressure and assume a 1.36 multiplying factor to include He (Elmegreen 1989). For the H II regions surrounding the clusters, we calculate the pressure contribution from photoionization, direct radiation pressure, and stellar winds. We do not include dust-reprocessed radiation pressure because our clusters have stellar surface densities $\lesssim 10^4\,M_{\odot}\,{\rm pc}^{-2}$, i.e., they are about an order of magnitude below the minimum stellar surface density for dust-reprocessed radiation pressure to significantly contribute to feedback (Krumholz et al. 2019). We consider the two extreme cases of a 25,000 $M_{\odot}$, 4 Myr stellar cluster with size 3 pc and a 3000 $M_{\odot}$, 6 Myr stellar cluster with size 1 pc to bracket the observed range of the dust-buried sources. For these two extreme cases, we use the Starburst99 ionizing photon fluxes to derive electron densities of 590 ${\rm cm}^{-3}$ and 350 ${\rm cm}^{-3}$, respectively, using a Strömgren sphere approximation. The electron densities in the H II regions are slightly lower than those derived for the gas surrounding them. The photoionization and direct radiation pressures are calculated using the formulae published by Lopez et al. (2014). For the photoionization, we get $P_{\rm ph}/k_B = 0.7–1.2 \times 10^7\,{\rm K\,cm}^{-3}$, while for the radiation pressure, $P_{\rm rad}/k_B = 2.4–4.4 \times 10^7\,{\rm K\,cm}^{-3}$. We derive the stellar wind pressure using the formula of Weaver et al. (1977) as formulated in Smith et al. (2006). We obtain that the bubble pressure is $P_{\rm wind}/k_B = 3.1–17.3 \times 10^7\,{\rm K\,cm}^{-3}$ for 100% thermal efficiency and $0.7–3.7 \times 10^7\,{\rm K\,cm}^{-3}$ for 10% thermal efficiency. Each of these pressure terms is comparable to or slightly larger (but only by a factor of a few) than the external pressure, supporting the inference above that the H II regions are not expanding and are likely to have stalled, due possibly to radiative cooling (Silich et al. 2007).

Smith et al. (2006) and Westmoquette et al. (2014) analyzed three clusters in the nearby starburst galaxy M 82 that appear to have encountered a fate similar to our dust-buried clusters. The spectroscopic ages of these three clusters, 4.5–6.4 Myr, are similar to those of the dust-buried stellar clusters found in this work. They have large attenuations, $E(B - V) \simeq 1.4–1.9$ mag, but significantly higher masses than our clusters, by a factor almost 100. Yet, these stellar clusters are also found to have stalled due to the high-pressure environment in the central region of M82. For comparison, Smith et al. (2006) and Westmoquette et al. (2014) determined values of the external pressure comparable to those we find. Similarly, Della Bruna et al. (2022) found that H II regions in the center of the starburst galaxy M83 are stalled because the ambient pressure is larger than the pre-SN pressure.

For completeness, we consider the possibility that, because our dust-buried clusters are young, relatively massive, and

compact, gas removal may be prevented by self-gravity (Krause et al. 2016, 2020). Krause et al. (2016) derived a relation between the compactness of a stellar cluster, defined as the mass/(half-mass radius), and the star formation efficiency. Clusters that form with sufficiently high efficiency at fixed compactness are effective at removing gas from their immediate surroundings. If we adopt our I-band half-light radius as a tracer of the half-mass–radius, the compactness of our clusters spans the range 0.6–$1.7 \times 10^4\,M_\odot\,\mathrm{pc}^{-1}$. For this range, self-gravity does not inhibit gas expulsion when star formation efficiencies are above 20%–30% (Krause et al. 2016). Although we do not have values for the star formation efficiency of our dust-buried stellar clusters, other estimates suggest this to be about 30% when evaluated at the sizes of clumps and clusters (e.g., Lada & Lada 2003; Calzetti et al. 2015a; Krumholz et al. 2019) and could increase with increasing stellar mass up to $\sim$60% at $10^6\,M_\odot$ (Turner et al. 2015). If these efficiencies are applicable to our dust-buried clusters, the impact of self-gravity at preventing gas clearance is expected to be secondary relative to the other effects discussed above.

We note that the population we identify is likely to be a lower limit to the full dusty population in the 5–6 Myr age range. Our sources are explicitly selected to have hydrogen recombination line emission. As we are at the boundary where stochastic sampling of the stellar IMF begins to become important, we expect larger numbers of dusty, 5–6 Myr stellar clusters to have been missed by our search due to the absence of line emission (Fumagalli et al. 2011). The addition of these clusters would only increase the dusty population and its implications for the lack of effectiveness of pre-SN feedback.

9. Summary and Conclusions

Using multiwavelength HST imaging data, which include NUV, optical, and near-IR, including narrowband filters centered at the hydrogen line emission of Hα and Paβ, we isolate a population of highly extincted stellar clusters, with $A_V \sim 6$–11 mag and ages $\sim$5–6 Myr. These clusters are numerous enough to be comparable to the low-dust cluster population identified using NUV-optical images in the same age and mass ranges (Adamo et al. 2017). Despite the similarity in numbers, however, the two populations possess morphologically distinct nebular emission properties: the low-dust clusters are consistent with early gas clearing, while the highly extincted clusters have retained their gas and show compact Paβ emission. We use this difference, together with other arguments, to exclude spurious effects, such as that the highly extincted clusters could have emerged behind the clouds where they formed; although we cannot exclude that at least some in our population are of this nature. The highly extincted clusters are, therefore, likely to be buried or partially buried in their natal clouds.

Stochastic sampling of the stellar IMF could have some effect on the derived ages, masses, and extinctions; although we present arguments, based on the spatial distribution of the dust-buried clusters, that exclude a large impact of stochasticity on our results. We also exclude direct absorption by dust of ionizing photons as a major driver for the relatively old ages we derive from SED fits. The dearth of clusters younger than $\sim$4 Myr in our sample can be understood in terms of our selection criteria, which require our sources to be simultaneously detected in all near-IR bands and undetected or marginally detected in all NUV and optical bands, including detection in the Paβ emission line and non/marginal detection in Hα.

The dust-buried clusters are sufficiently old that pre-SN feedback should have already cleared the natal cloud; however, the amount of dust in front of the clusters indicates that pre-SN feedback has not been effective. Furthermore, the surrounding gas has sufficiently high pressure and density that the H II regions around the clusters are likely to have been stalled. These lines of evidence paint a scenario for which a significant fraction of clusters in the mass range 0.3–$2.5 \times 10^4\,M_\odot$ do not emerge from their dust clouds in a short timescale, but remain within the cloud for at least 6 Myr. Such a finding challenges models that require pre-SN feedback to be highly effective at clearing the natal clouds in order to keep the star formation efficiency low and suggests that the pressure from the natal cloud plays an important role in determining the timescale for such clearing. Upcoming JWST observations of this and other galaxies, especially targeting the infrared emission of hydrogen recombination lines, will be key for providing a more complete picture of the nature of dusty stellar cluster populations.

ORCID iDs

Daniela Calzetti ⬤ https://orcid.org/0000-0002-5189-8004
Sean T. Linden ⬤ https://orcid.org/0000-0002-1000-6081
Matteo Messa ⬤ https://orcid.org/0000-0003-1427-2456

Zhiyuan Ji ⓘ https://orcid.org/0000-0001-7673-2257
Mark R. Krumholz ⓘ https://orcid.org/0000-0003-3893-854X
Angela Adamo ⓘ https://orcid.org/0000-0002-8192-8091
Bruce Elmegreen ⓘ https://orcid.org/0000-0002-1723-6330
Kathryn Grasha ⓘ https://orcid.org/0000-0002-3247-5321
Kelsey E. Johnson ⓘ https://orcid.org/0000-0001-8348-2671
Elena Sabbi ⓘ https://orcid.org/0000-0003-2954-7643
Linda J. Smith ⓘ https://orcid.org/0000-0002-0806-168X

References

Adamo, A., Östlin, G., Zackrisson, E., et al. 2010, MNRAS, 407, 870
Adamo, A., Ryon, J. E., Messa, M., et al. 2017, ApJ, 841, 131
Asplund, M., Grevesse, N., Sauval, A. J., & Scott, P. 2009, ARA&A, 47, 481
Bending, T. J. R., Dobbs, C. L., & Bate, M. R. 2022, MNRAS, 513, 2088
Berg, D. A., Skillman, E. D., Marble, A. R., et al. 2012, ApJ, 754, 98
Bessell, M. S. 2005, ARA&A, 43, 293
Bohlin, R. C., Savage, B. D., & Drake, J. F. 1978, ApJ, 224, 132
Brown, G., & Gnedin, O. Y. 2021, MNRAS, 508, 5935
Calzetti, D. 2001, PASP, 113, 1449
Calzetti, D., Armus, L., Bohlin, R. C., et al. 2000, ApJ, 533, 682
Calzetti, D., Battisti, A. J., Shivaei, I., et al. 2021, ApJ, 913, 37
Calzetti, D., Johnson, K. E., Adamo, A., et al. 2015a, ApJ, 811, 75
Calzetti, D., Kennicutt, R. C., Engelbracht, C. W., et al. 2007, ApJ, 666, 870
Calzetti, D., Kinney, A. L., & Storchi-Bergmann, T. 1994, ApJ, 429, 582
Calzetti, D., Lee, J. C., Sabbi, E., et al. 2015b, AJ, 149, 51
Calzetti, D., Wilson, G. W., Draine, B. T., et al. 2018, ApJ, 852, 106
Castelli, F., & Kurucz, R. L. 2003, in IAU Symp. 210, Modelling of Stellar Atmospheres, ed. N. Piskunov, W. W. Weiss, & D. F. Gray (San Francisco, CA: ASP), A20
Cerviño, M., Valls-Gabaud, D., Luridiana, V., & Mas-Hesse, J. M. 2002, A&A, 381, 51
Chevance, M., Kruijssen, J. M. D., Krumholz, M. R., et al. 2022, MNRAS, 509, 272
Choi, J., Dotter, A., Conroy, C., et al. 2016, ApJ, 823, 102
Conroy, C., & Gunn, J. E. 2010, ApJ, 712, 833
Conroy, C., Gunn, J. E., & White, M. 2009, ApJ, 699, 486
Cook, D. O., Dale, D. A., Johnson, B. D., et al. 2014, MNRAS, 445, 899
Corbelli, E., Braine, J., Bandiera, R., et al. 2017, A&A, 601, A146
Dale, J. E., Ercolano, B., & Bonnell, I. A. 2012, MNRAS, 424, 377
Davies, B., Kudritzki, R.-P., Plez, B., et al. 2013, ApJ, 767, 3
de Vaucouleurs, G., de Vaucouleurs, A., Corwin, H. G., Jr., et al. 1991, Third Reference Catalogue of Bright Galaxies (Berlin: Springer)
Della Bruna, L., Adamo, A., McLeod, A. F., et al. 2022, A&A, 666, A29
Dinnbier, F., & Walch, S. 2020, MNRAS, 499, 748
Dobbs, C. L. 2015, MNRAS, 447, 3390
Dobbs, C. L., Burkert, A., & Pringle, J. E. 2011, MNRAS, 417, 1318
Dopita, M. A., Groves, B. A., Sutherland, R. S., & Kewley, L. J. 2003, ApJ, 583, 727
Dotter, A. 2016, ApJS, 222, 8
Draine, B. T. 2011, ApJ, 732, 100
Elmegreen, B. G. 1989, ApJ, 338, 178
Falcón-Barroso, J., Sánchez-Blázquez, P., Vazdekis, A., et al. 2011, A&A, 532, A95
Federrath, C. 2015, MNRAS, 450, 4035
Ferland, G. J., Porter, R. L., van Hoof, P. A. M., et al. 2013, RMxAA, 49, 137
Fitzpatrick, E. L. 1999, PASP, 111, 63
Fitzpatrick, E. L., Massa, D., Gordon, K. D., Bohlin, R., & Clayton, G. C. 2019, ApJ, 886, 108
Fumagalli, M., da Silva, R. L., & Krumholz, M. R. 2011, ApJL, 741, L26
Girardi, L., Bressan, A., Bertelli, G., & Chiosi, C. 2000, A&AS, 141, 371
Goldbaum, N. J., Krumholz, M. R., & Forbes, J. C. 2016, ApJ, 827, 28
Gonzaga, S., Hack, W., Fruchter, A., & Mack, J. 2012, The DrizzlePac Handbook (Baltimore, MD: STScI)
Gordon, K. D., Calzetti, D., & Witt, A. N. 1997, ApJ, 487, 625
Gordon, K. D., Clayton, G. C., Misselt, K. A., Landolt, A. U., & Wolff, M. J. 2003, ApJ, 594, 279
Gordon, K. D., Meixner, M., Meade, M. R., et al. 2011, AJ, 142, 102
Grasha, K., Calzetti, D., Adamo, A., et al. 2019, MNRAS, 483, 4707
Grasha, K., Calzetti, D., Andrews, J. E., Lee, J. C., & Dale, D. A. 2013, ApJ, 773, 174
Grasha, K., Calzetti, D., Bittle, L., et al. 2018, MNRAS, 481, 1016
Greissl, J., Meyer, M. R., Christopher, M. H., & Scoville, N. Z. 2010, ApJ, 710, 1746

Grisdale, K., Agertz, O., Romeo, A. B., Renaud, F., & Read, J. I. 2017, MNRAS, 466, 1093
Grudić, M. Y., Guszejnov, D., Offner, S. S. R., et al. 2022, MNRAS, 512, 216
Grudić, M. Y., Hopkins, P. F., Faucher-Giguère, C.-A., et al. 2018, MNRAS, 475, 3511
Hannon, S., Lee, J. C., Whitmore, B. C., et al. 2019, MNRAS, 490, 4648
Hannon, S., Lee, J. C., Whitmore, B. C., et al. 2022, MNRAS, 512, 1294
Hao, C.-N., Kennicutt, R. C., Johnson, B. D., et al. 2011, ApJ, 741, 124
Hennebelle, P., & Chabrier, G. 2011, ApJL, 743, L29
Hollyhead, K., Bastian, N., Adamo, A., et al. 2015, MNRAS, 449, 1106
Holwerda, B. W., Keel, W. C., & Bolton, A. 2007, AJ, 134, 2385
Hopkins, P. F., Grudić, M. Y., Wetzel, A., et al. 2020, MNRAS, 491, 3702
Hopkins, P. F., Kereš, D., Oñorbe, J., et al. 2014, MNRAS, 445, 581
Hopkins, P. F., Quataert, E., & Murray, N. 2012, MNRAS, 421, 3488
Hunter, D. A., Elmegreen, B. G., Dupuy, T. J., & Mortonson, M. 2003, AJ, 126, 1836
Hunter, D. A., Rubin, V. C., Swaters, R. A., Sparke, L. S., & Levine, S. E. 2005, ApJ, 634, 281
Hunter, D. A., Wilcots, E. M., van Woerden, H., Gallagher, J. S., & Kohle, S. 1998, ApJL, 495, L47
Johnson, B. D., Leja, J., Conroy, C., & Speagle, J. S. 2021, ApJS, 254, 22
Johnson, K. E., Hunt, L. K., & Reines, A. E. 2009, AJ, 137, 3788
Johnson, K. E., & Kobulnicky, H. A. 2003, ApJ, 597, 923
Johnson, K. E., Kobulnicky, H. A., Massey, P., & Conti, P. S. 2001, ApJ, 559, 864
Joye, W. A., & Mandel, E. 2003, in ASP Conf. Ser. 295, Astronomical Data Analysis Software and Systems XII, ed. H. E. Payne, R. I. Jedrzejewski, & R. N. Hook (San Francisco, CA: ASP), 489
Kepley, A. A., Reines, A. E., Johnson, K. E., & Walker, L. M. 2014, AJ, 147, 43
Kim, J., Chevance, M., Kruijssen, J. M. D., et al. 2021, MNRAS, 504, 487
Kim, J., Chevance, M., Kruijssen, J. M. D., et al. 2023, ApJL, 944, L20
Kobulnicky, H. A., & Johnson, K. E. 1999, ApJ, 527, 154
Krause, M., Fierlinger, K., Diehl, R., et al. 2013, A&A, 550, A49
Krause, M. G. H., Charbonnel, C., Bastian, N., & Diehl, R. 2016, A&A, 587, A53
Krause, M. G. H., Offner, S. S. R., Charbonnel, C., et al. 2020, SSRv, 216, 64
Kreckel, K., Groves, B., Schinnerer, E., et al. 2013, ApJ, 771, 62
Kroupa, P. 2001, MNRAS, 322, 231
Kruijssen, J. M. D., Schruba, A., Chevance, M., et al. 2019, Natur, 569, 519
Krumholz, M. R., Adamo, A., Fumagalli, M., et al. 2015, ApJ, 812, 147
Krumholz, M. R., & Matzner, C. D. 2009, ApJ, 703, 1352
Krumholz, M. R., & McKee, C. F. 2005, ApJ, 630, 250
Krumholz, M. R., McKee, C. F., & Bland-Hawthorn, J. 2019, ARA&A, 57, 227
Lada, C. J., & Lada, E. A. 2003, ARA&A, 41, 57
Lada, C. J., Lombardi, M., & Alves, J. F. 2009, ApJ, 703, 52
Lançon, A., Hauschildt, P. H., Ladjal, D., & Mouhcine, M. 2007, A&A, 468, 205
Lawton, B., Gordon, K. D., Babler, B., et al. 2010, ApJ, 716, 453
Lee, J. C., Gil de Paz, A., Tremonti, C., et al. 2009, ApJ, 706, 599
Leitherer, C., Ekström, S., Meynet, G., et al. 2014, ApJS, 212, 14
Leitherer, C., Schaerer, D., Goldader, J. D., et al. 1999, ApJS, 123, 3
Lelli, F., Verheijen, M., & Fraternali, F. 2014, MNRAS, 445, 1694
Linden, S. T., Evans, A. S., Armus, L., et al. 2023, ApJL, 944, L55
Lopez, L. A., Krumholz, M. R., Bolatto, A. D., et al. 2014, ApJ, 795, 121
Lucas, W. E., Bonnell, I. A., & Dale, J. E. 2020, MNRAS, 493, 4700
Ma, X., Quataert, E., Wetzel, A., et al. 2020, MNRAS, 498, 2001
Matthews, A. M., Johnson, K. E., Whitmore, B. C., et al. 2018, ApJ, 862, 147
Meixner, M., Gordon, K., Indebetouw, R., et al. 2006, AJ, 132, 2268
Messa, M., Calzetti, D., Adamo, A., et al. 2021, ApJ, 909, 121
Meynet, G., Maeder, A., Schaller, G., Schaerer, D., & Charbonnel, C. 1994, A&AS, 103, 97
Oestreicher, M. O., Schmidt-Kaler, T., & Wargau, W. 1997, MNRAS, 289, 729
Oey, M. S., King, N. L., & Parker, J. W. 2004, AJ, 127, 1632
Orr, M. E., Hayward, C. C., Hopkins, P. F., et al. 2018, MNRAS, 478, 3653
Osterbrock, D. E., & Ferland, G. J. 2006, Astrophysics of Gaseous Nebulae and Active Galactic Nuclei (Mill Valley, CA: Univ. Science Books)
Ostriker, E. C., & Kim, C.-G. 2022, ApJ, 936, 137
Ostriker, E. C., McKee, C. F., & Leroy, A. K. 2010, ApJ, 721, 975
Pellegrini, E. W., Baldwin, J. A., & Ferland, G. J. 2011, ApJ, 738, 34
Peters, T., Naab, T., Walch, S., et al. 2017, MNRAS, 466, 3293
Pilyugin, L. S., Grebel, E. K., & Zinchenko, I. A. 2015, MNRAS, 450, 3254
Reines, A. E., Johnson, K. E., & Goss, W. M. 2008, AJ, 135, 2222
Rémy-Ruyer, A., Madden, S. C., Galliano, F., et al. 2014, A&A, 563, A31

Ryon, J. E., Gallagher, J. S., Smith, L. J., et al. 2017, ApJ, 841, 92
Schlafly, E. F., & Finkbeiner, D. P. 2011, ApJ, 737, 103
Schneider, S. E., Thuan, T. X., Mangum, J. G., & Miller, J. 1992, ApJS, 81, 5
Sewiło, M., Carlson, L. R., Seale, J. P., et al. 2013, ApJ, 778, 15
Silich, S., Tenorio-Tagle, G., & Muñoz-Tuñón, C. 2007, ApJ, 669, 952
Smith, L. J., Westmoquette, M. S., Gallagher, J. S., et al. 2006, MNRAS, 370, 513
Sokal, K. R., Johnson, K. E., Indebetouw, R., & Reines, A. E. 2015, AJ, 149, 115
Speagle, J. S. 2020, MNRAS, 493, 3132
Stark, D. P., Ellis, R. S., Bunker, A., et al. 2009, ApJ, 697, 1493
Tody, D. 1986, Proc. SPIE, 627, 733
Tody, D. 1993, in ASP Conf. Ser. 52, Astronomical Data Analysis Software and Systems II, ed. R. J. Hanisch, R. J. V. Brissenden, & J. Barnes (San Francisco, CA: ASP), 173
Tully, R. B., Courtois, H. M., Dolphin, A. E., et al. 2013, AJ, 146, 86
Turner, J. L., & Beck, S. C. 2004, ApJL, 602, L85
Turner, J. L., Beck, S. C., Benford, D. J., et al. 2015, Natur, 519, 331

Vázquez, G. A., & Leitherer, C. 2005, ApJ, 621, 695
Weaver, R., McCray, R., Castor, J., Shapiro, P., & Moore, R. 1977, ApJ, 218, 377
Westmoquette, M. S., Bastian, N., Smith, L. J., et al. 2014, ApJ, 789, 94
Whitaker, K. E., van Dokkum, P. G., Brammer, G., & Franx, M. 2012, ApJL, 754, L29
Whitmore, B. C., Chandar, R., Jimena Rodríguez, M., et al. 2023, ApJL, 944, L14
Whitmore, B. C., Chandar, R., Kim, H., et al. 2011, ApJ, 729, 78
Whitmore, B. C., Chandar, R., Lee, J., et al. 2020, ApJ, 889, 154
Whitney, B. A., Sewilo, M., Indebetouw, R., et al. 2008, AJ, 136, 18
Yeh, S. C. C., Verdolini, S., Krumholz, M. R., Matzner, C. D., & Tielens, A. G. G. M. 2013, ApJ, 769, 11
Zackrisson, E., Rydberg, C.-E., Schaerer, D., Östlin, G., & Tuli, M. 2011, ApJ, 740, 13
Zamora-Avilés, M., Vázquez-Semadeni, E., González, R. F., et al. 2019, MNRAS, 487, 2200
Zhu, H., Tian, W., Li, A., & Zhang, M. 2017, MNRAS, 471, 3494